Development of a Digital Volume Correlation Framework for Analyzing Deformations in Axially Loaded Meniscus Samples

Mikael Lilja

Master's Thesis in
Biomedical Engineering

Faculty of Engineering, LTH
Department of Biomedical Engineering

Main supervisor: Maria Pierantoni
Assistant supervisors: Lorenzo Grassi and Hanna Isaksson

Title
Development of a Digital Volume Correlation Framework for Analyzing Deformations in Axially Loaded Meniscus Samples

Author
Mikael Lilja

Figures
Created by the author if nothing else is indicated

Acknowledgements

Abstract

The knee menisci distribute and dampen mechanical loads. Vulnerability to injury and disease of the meniscus is a global issue, particularly concerning osteoarthritis. The connection between the breakdown of meniscal tissue and its mechanical response is not entirely understood. This thesis seeks to contribute to filling this knowledge gap by developing and implementing a digital volume correlation (DVC) procedure to compute strains from synchrotron-based phase-contrast-enhanced tomograms of meniscus samples acquired during an unconfined mechanical test with stress relaxation.

A comparative analysis was conducted between two algorithms, one classic implementation of DVC and one based on the augmented Lagrangian method. The latter algorithm was then selected for the dynamic data based on its stronger performance. By performing parameter optimization, noise reduction and other adaptions to the data, displacements and strains were computed across four deformation states for two menisci of different health conditions. The outcomes were validated by studying the deformation residual convergences of the optimization routine, assessment of the signal-to-noise ratios, and by manual measurement controls.

Quantitative analysis of the results revealed significant differences in average node strains between meniscus samples during load and relaxation. As expected a weaker Poisson's effect was obtained for the visually degenerated sample. The most pronounced distinction was observed in the secondary, viscoelastic response, where the visually healthy meniscus displayed a more efficient relaxation process. This was manifested in correlation results with the volume acquired immediately after load as reference, particularly in the direction of loading where mean absolute normal strains after 100 s and 900 s of relaxation were 136% and 107% higher than in the degenerated meniscus.

The results of this thesis showed that Augmented Lagrangian Digital Volume Correlation (ALDVC) provides sufficiently accurate strains from the given meniscus data. The findings were in alignment with earlier knowledge of how mechanical properties of menisci change with degeneration. Moving forward, more menisci samples should be studied and at a higher frequency of time intervals to gain a more comprehensive understanding of the mechanical response.

List of acronyms & abbreviations

- μCT - micro-Computed Tomography

- SXR-PhC-μCT - Synchrotron X-ray Radiation based Phase Contrast enhanced micro-Computed Tomography

- E - Elastic modulus

- OA - Osteoarthritis

- DVC - Digital Volume Correlation

- ALDVC - Augmented Lagrangian Digital Volume Correlation

- ADMM - Alternating Direction Method of Multipliers

- ICGN - Inverse Compositional Gauss-Newton

- CW - Correlation Window

- SW - Search Window

- NS - Node Spacing

- VOI - Volume of Interest

- RMSE - Root Mean Square Error

Contents

Chapter 1

Introduction

The knee menisci are paired, crescent-shaped fibrocartilaginous structures located at the medial and lateral positions of the knee joint. They consist of mostly water and collagen and serve various functions within the knee such as load distribution, shock absorption, and lubrication assistance. The collagenous fiber structure of the meniscus is of fundamental importance for these processes. A majority of the fibers are oriented in the longitudinal and circumferential direction or interwoven with obliquely angled fibers. Additionally, the superficial layer exhibits a random fiber orientation [1].

The meniscus is susceptible to injury and disease. Osteoarthritis (OA) is a degenerative joint disease characterized by the gradual breakdown of cartilage. It also impacts the bone and, in the case of the knee, the meniscus, where it is associated with damage to the collagen structure [1], [2]. This can lead to the occurrence of meniscal tears, which conversely more frequently contribute to the development of OA [3]. Osteoarthritis is the 11th most debilitating condition on a global scale, and the social and economic implications stemming from perceived pain and reduced joint functionality are substantial [4]. Moreover, it is anticipated that the incidence of OA will continue to rise, due to ongoing trends like an aging population and escalating rates of obesity [5]. The breakdown of cartilage and meniscal tissue may be linked to impaired mechanical response. However, the connection between this response and the meniscus structure remains not entirely understood.

Micro-computed tomography (μCT) is a powerful imaging technique capable of producing high-resolution 3D images. To enable fast acquisitions for in situ mechanical loading experiments, synchrotron radiation-based μCT is preferred. In turn, the utilization of a synchrotron light source provides the option to use phase-contrast enhancement (PhC) to improve the contrast of low x-ray absorbing materials without requiring the use of contrast agents [6]. Non-mineralized biological tissue such as the meniscus is characterized by low absorption and avoiding the use of contrast agents is essential to preserve the native mechanical properties during in situ tests [7].

The mechanical behavior of the meniscus after an applied external force, in the form of strains can be determined using digital volume correlation (DVC). DVC is a non-contact method to track deformations by examining the pixel intensity matching between small sub-volumes of volumetric images, before and after loading, to generate a comprehensive

3D motion field. There are many factors that can impact the accuracy of DVC measurements, including the dimensions of the subset window used in the matching process of points between volumes captured at different time points, and the choice of data smoothing techniques [8]. In the biomechanics field, DVC has been used for measuring strains in, for instance, intervertebral discs and bone but has not yet been applied to meniscus volumes [9], [10].

1.1 Objectives

This project aims to quantify displacements and strains within the meniscus when subjected to uniaxial, unconfined compression, through digital volume correlation. Available volumes are synchrotron X-ray computed tomographs with propagation-based phase contrast enhancement, acquired during a two step stress-relaxation test with 15% and 30% strain. The first goal of the project involves an investigation of the performance of two different DVC algorithms, TomoWarp2 and ALDVC, in a static scenario to determine their potential in the specific case of our experimental data. The next goal is to use at least one of the algorithms for the loaded sample volumes to compute strains, by careful configuration of crucial parameters and other algorithmic settings. The validity of the outcomes will be investigated, and a comparison will be conducted among menisci in different health states.

Chapter 2

Background

2.1   Knee

The knee is composed of the lateral and medial femorotibial and the femorapatellar articulations. This makes it the largest and most complex joint in the body [11]. The complexity allows for a wide range of movements and contributes to the health of the articulation, but it also makes it prone to injury and susceptible to diseases. One of the pivotal components within the knee joint organ is the meniscus [1].
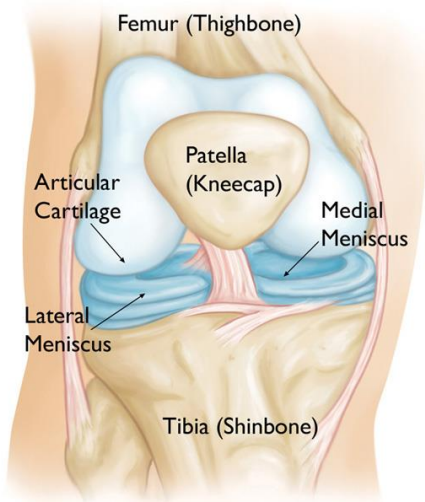
(a) Anatomy of the knee [12].
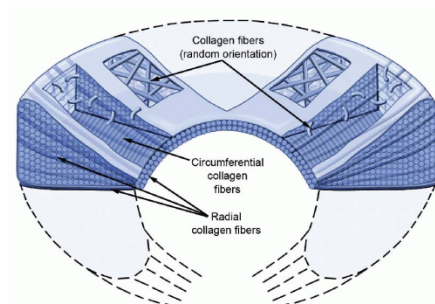
(b) Fiber structure of the meniscus [13].

Figure 2.1

2.2 Meniscus

2.2.1 Structure

The human meniscus consists of two crescent-shaped wedges located in the medial and the lateral part of the knee, between the femoral and tibial condyles, respectively (Figure 2.1a. The superior surface of the meniscus is concave to fit the convex femoral condyles while the inferiors are flat to match the tibial plateau. It is an extracellular fibrocartilagenous matrix that consists of 72% water and 22% collagen, and other noncollagenous proteins such as proteoglycans, and glycoproteins. The tissue contains spindle-shaped fusiform cells closer to the surface and oval-shaped ovoid cells deeper inside. These cells play a crucial role in preserving the strength and structure of the meniscus [14].

Type I collagen dominates the collagen composition in the meniscus, making up around 90% of the total collagen content. Other types, present in smaller quantities, are collagen II, III, V, and VI [14]. Tropocollagen molecules are the elemental components in collagen, which combine into nanostructural-collagen fibrils in a helix-shaped manner [15]. The organization of fibrils into fibers and bundles of fibers further occurs at the micro-scale [16].

2.2.2 Mechanical properties

The meniscus is an important component for the biomechanics of the knee joint. Its main functions are load transmission, shock absorption, lubrication, and, to a smaller extent, nutritional transport [14]. It plays a role in the minimization of stress on the cartilage, and serves as a secondary stabilizer of the knee, following the role of the ligaments. The lateral meniscus helps in preventing revolving movements whereas the medial meniscus mainly supports anteroposterior translation [17]. The meniscus is also viscoelastic, primarily influenced by its water content. This property results in effective shock absorption, as the movement of tissue fluid generates frictional drag forces [18].

The type I collagen fibers and fiber bundles are vital structural elements for the tissue. They are oriented circumferentially and play a major part in transmitting compressive forces from the femur into tensile forces in a load distribution process. These longitudinally oriented fibers are interlaced with radially directed fibers which maintain the structure during loading by preventing outward displacement (Figure 2.1b) [1]. While these specifically oriented fibers are located in the inner parts, there is also a superficial, thin layer with fibers constituting a random meshwork.

Stiffness of the meniscal fiber structure is hierarchical in the sense that it decreases with the increasing component scale. For the basic tropocollagen units, values of the Elastic modulus, E, have been estimated to 2.9-9 GPa in tension [15]. For fibers, $E = 0.1$-0.4 GPa, and for the whole meniscus it holds that $E = \sim 0.1$ GPa. The decrease in stiffness shows an inverse relationship with the number of deformation mechanisms [19], [20] .

Circumferential tension in the meniscus is a nonlinear process, even though the fibers themselves show mostly linear mechanical behavior. The nonlinearity is due to a stage of initial fiber response by uncrimping or rotation into the load direction [21]. When most of the

fibers are uncrimped the tension enters a linear phase. This rarely occurs at strain levels above 10%. The transition from linear elasticity to plasticity commonly occurs at higher strains ($20 \sim 30\%$) [22].

2.3   Osteoarthritis

Osteoarthritis (OA) is a common degenerative joint ailment, impacting a significant part of the population, with an estimated 16% of men and 29% of women in Europe aged 55 or older being affected. The resulting pain and reduced functionality have notable social and economic implications [4], [23]. Around 3% of the global population is affected by OA, leading to moderate to critical disability in 43 million people. This ranks it as the 11th most debilitating condition on a global scale [24].

The disease is most commonly found in the knees, hands, hips, and spine. It is a chronic condition that causes predominantly the cartilage in the joint to deteriorate. Besides age and sex, several factors can influence the initiation of OA such as heredity, obesity, injury, and joint overuse. Some of the symptoms of the disease include pain, stiffness, muscle weakness, swelling and reduced range of motion [25]. Traditional treatments mainly address pain management and, in severe cases, joint replacement. However, recent advances in understanding the disease process and improved methods for assessing disease activity are driving a shift toward preventing and treating early osteoarthritis [4].

In knee osteoarthritis, damage to the meniscus is very frequent. Such damage can manifest as flap or horizontal tears, meniscal maceration, or complete destruction. The relationship between meniscal tears and knee OA is bidirectional. A meniscal tear can lead to the development of OA, and knee OA can also result in spontaneous meniscal tears. The presence of a degenerative meniscal lesion often indicates early stages of knee OA [3].

2.4   X-ray Computed Tomography

2.4.1   X-ray imaging

In X-ray scanning, X-rays pass through a sample and are detected on the other side using a detector. The process relies on recording the varying transmission of electromagnetic waves through the sample. The X-rays are generated by a source, such as a traditional X-ray tube or a synchrotron, through the interaction of high-energy electrons with a metal target [26],[27]. In a two-dimensional object representation, the contrasts indicate the absorptions of different structures along the beam axis. The spatial distribution of intensities provides information about the shapes and fine structures of the sample perpendicular to the beam axis [28].

2.4.2 Computed tomography

X-ray computed tomography (CT) involves acquiring a sequence of 2D X-ray projections of an object from various angles. By reconstructing the projections in 3D volumes, a detailed 3D representation of the scanned object is created. This non-destructive technique enables us to explore the interior of objects. It furthermore generates contrast among different material types, which are determined by their respective compositions and densities. Specifically, a μCT scanner is tailored for high-resolution of small objects, typically ranging from 1mm to 20cm in diameter. This results in resolutions of 1 to 70 micrometers [29].

While CT is primarily used in medical imaging, μCT finds application across a broader spectrum of scientific fields, including biological, geological, and material sciences [30]. In conventional CT, the source and detector rotate around the sample or body. In μCT, on the other hand, the sample itself rotates while the imaging system remains fixed [31]. This design facilitates the image resolution adjustment for smaller samples, which can be made by changing distances between the object, source, and detector. In addition, μCT offers greater flexibility compared to standard CT regarding voltage and current modification, which allows the setup to be altered to accommodate a variety of materials [30].

2.4.3 Synchrotron-based phase contrast enhancement

A synchrotron X-ray (SXR) is a type of X-ray radiation produced using a synchrotron particle accelerator. SXR tomography offers several benefits compared to traditional X-ray radiation, making it a valuable tool in biomedical imaging. These advantages include its high intensity, the ability to tune X-ray energy, and a strong natural collimation [32]. The X-rays can also be rendered monochromatic through the use of a monochromator [33]. The precise beam control can reduce background signal stemming from scattered photons. Furthermore, the elevated speed of image acquisition and high resolution facilitates the potential for real-time imaging of small, dynamic, in-motion samples [34].

Non-mineralized tissue like the meniscus is characterized by low absorption which results in low x-ray imaging contrast [35]. Normally, contrast agents are necessary for conventional laboratory CT scans of low-absorption materials. However, the utilization of a synchrotron light source provides the option to use phase-contrast enhancement (PhC), which improves soft tissue contrast without the need for contrast agents. The use of SXR-PhC-μCT combines the benefits of a synchrotron source and PhC, which allows for the individual visualization of fibers and fiber bundles within the meniscus [6]. Unlike regular tomographic methods, which mainly depend on X-ray absorption, phase contrast enhancement takes advantage of the refraction of X-rays by matter. The phase shift caused by the sample is not directly measured but is instead transformed into variations in intensity. These variations can then be recorded by the detector, enabling the visualization of features with limited X-ray absorption [36], [37]. An arrangement for an SXR-PhC-μCT experiment is shown in Figure 2.2.

2.5 Mechanical response

During compression tests, force and displacement data are recorded to generate stress-strain curves. Compressive testing offers numerous advantages, and the most notable is that it al-
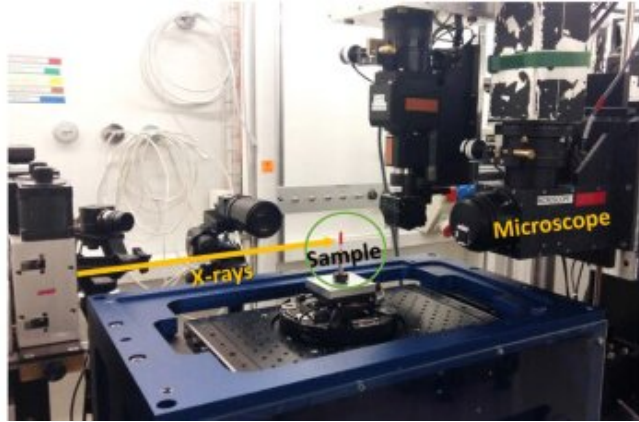
Figure 2.2: An SXR-PhC-μCT imaging set-up from the TOMCAT beamline of the Swiss Light Source, obtained at an experiment where the feasibility of SXR-PhC-μCT for meniscus imaging was studied [6].

lows for the evaluation of soft tissues under physiologically relevant loads within a hydrated environment. Testing load-bearing tissues through compression is crucial as many tissues in the body experience compressive forces. This approach improves the accuracy of measuring their mechanical properties [38].

The mechanical response of the sample is studied by examining its stresses and strains. The stress vector $\mathbf{s}$ in a point is defined as $\mathbf{s} = \lim_{\Delta S \to 0} \frac{\Delta \mathbf{P}}{\Delta S}$, for a force $\Delta \mathbf{P}$ acting on a surrounding cross-sectional area ΔS. The component perpendicular to the cut surface is referred to as the normal stress σ, while the component parallel to the cut surface is termed the shear stress τ. Strains are divided into normal strains and shear strains. A normal strain ϵ is defined as the relative increase in length of a section of the given material under load, while the shear strain γ is defined as the change in the angle between two lines originally perpendicular to each other in the initial state [39].

The material-specific connection between stresses and strains can be established through the mechanical test. Figure 2.3 illustrates a loaded sample and a characteristic curve derived from the test. Until reaching the yield point σ_y, a linear relationship follows Hooke's law, expressed as $\sigma = E\epsilon$, where E represents the material's modulus of elasticity. The sample deforms without incurring any permanent changes during this phase and will regain its original shape once the stress is removed. Beyond the yield point, plastic deformation initiates which is non-reversible. Another parameter to quantify is Poisson's ratio, ν. It is a measure of the Poisson effect, the phenomenon in which a material tends to expand in directions perpendicular to the direction of compression. For isotropic materials and normal strains $\epsilon_{xx}, \epsilon_{yy}$, and ϵ_{zz}, the relation manifests as $\epsilon_{xx} = \epsilon_{yy} = -\nu \cdot \epsilon_{zz}$. In anisotropic materials like the meniscus on the other hand, ν generally differs in the transversal x and y directions [39], [40].

(a) A sample experiencing applied pressure indicated by the arrow.

(b) The relationship between stresses and strains in a sample during testing [41].
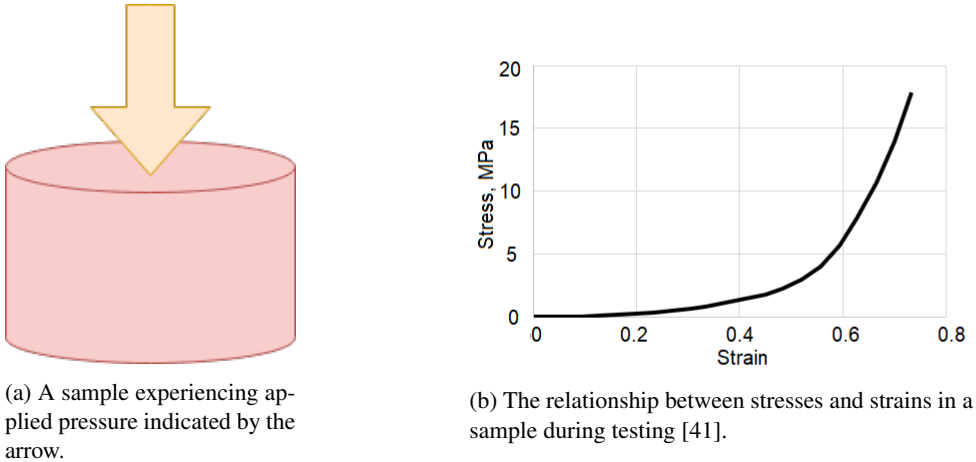
Figure 2.3: Unconfined compression test.

Understanding strains is integral for the characterization of the extent of compression, distortion, and stretching in a solid material exposed to external forces. Strains can emerge from a combination of rotational and translational movements, requiring us to distinguish this physical deformation from rigid motion. The infinitesimal strain tensor is applicable for moderate deformations within the elastic regime. Given a three dimensional displacement vector $\mathbf{u} = [u, v, w]$, the infinitesimal strain matrix is

$$\boldsymbol{\epsilon} = \frac{1}{2}(\nabla\mathbf{u} + (\nabla\mathbf{u})^T) = \begin{bmatrix} \frac{\partial u}{\partial x} & \frac{1}{2}(\frac{\partial u}{\partial y} + \frac{\partial v}{\partial x}) & \frac{1}{2}(\frac{\partial u}{\partial z} + \frac{\partial w}{\partial x}) \\ \frac{1}{2}(\frac{\partial u}{\partial y} + \frac{\partial v}{\partial x}) & \frac{\partial v}{\partial y} & \frac{1}{2}(\frac{\partial v}{\partial z} + \frac{\partial w}{\partial y}) \\ \frac{1}{2}(\frac{\partial u}{\partial z} + \frac{\partial w}{\partial x}) & \frac{1}{2}(\frac{\partial v}{\partial z} + \frac{\partial w}{\partial y}) & \frac{\partial w}{\partial z} \end{bmatrix}.$$

This symmetric matrix has diagonal elements $\epsilon_{xx} = \frac{\partial u}{\partial x}, \epsilon_{yy} = \frac{\partial v}{\partial y}$ and $\epsilon_{zz} = \frac{\partial v}{\partial z}$ corresponding to normal strains, which describe the elognation or compression of the material along its principal exes. The elements outside the diagonal, $\epsilon_{xy} = \frac{1}{2}(\frac{\partial u}{\partial y} + \frac{\partial v}{\partial x}), \epsilon_{yz} = \frac{1}{2}(\frac{\partial v}{\partial z} + \frac{\partial w}{\partial y})$, and $\epsilon_{xz} = \frac{1}{2}(\frac{\partial u}{\partial z} + \frac{\partial w}{\partial x})$, represent shear strains. They signify the material's distortion while preserving its volume and are associated with its resistance to shearing forces, which causes a change in shape [42].

2.6 Digital volume correlation

Digital volume correlation (DVC) is a non-contact method to calculate deformations and strains. It is the three-dimensional extension of digital image correlation, which first formulations as a method to track deformations can be traced to the 1980s. Specimen volumes acquired at different loading stages during mechanical testing form the basis of DVC. The working principle is to create a displacement field by maximizing a correlation coefficient for a chosen number of subsets distributed through the two volumes. The correlation maximization is done by examining the voxel intensity matching between volumes [8].
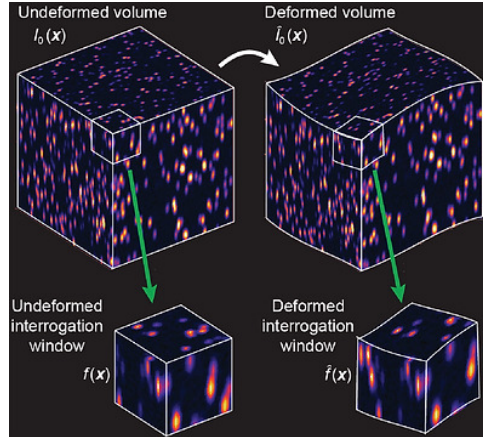
Figure 2.4: Fundamentals of digital volume correlation [44].

Mathematically, the problem can be formulated as

$$\max_{\mathbf{y}:\Omega\to\mathbb{R}^3} C_{CC} = \sum_{\mathbf{X}\in\Omega} f(\mathbf{X})g(\mathbf{y}(\mathbf{X})), \tag{2.1}$$

where $\mathbf{y}$ is the coordinate transformation of the original image f with voxel coordinates $\mathbf{X}$ in domain $\Omega \in \mathbb{R}^3$, resulting in the image $g(\mathbf{y}(\mathbf{X}))$. Thus, DVC is the inverse problem of uniquely finding the mapping from image $f(\mathbf{X})$ to the deformed image $g(\mathbf{y})$. By image sub-voxel interpolation the sum can be replaced by an integral which permits continuous, non-linear optimization:

$$\max_{\mathbf{y}:\Omega\to\mathbb{R}^3} C_{CC} = \int_{\Omega} f(\mathbf{X})g(\mathbf{y}(\mathbf{X}))\, d\mathbf{X}, \tag{2.2}$$

and an equivalent problem formulation is the minimization of the sum of squared differences:

$$\min_{\mathbf{y}:\Omega\to\mathbb{R}^3} C_{SSD} = \int_{\Omega} |f(\mathbf{X}) - g(\mathbf{y}(\mathbf{X}))|^2\, d\mathbf{X}. \tag{2.3}$$

DVC methods can typically be categorized in local and global methods. In a local DVC approach, the volume of interest (VOI) is subdivided into subsets, and the central point is commonly selected as the reference node. These subvolumes are then tracked between the original and the deformed volumetric images, and each volume-matching problem is solved independently. On the contrary, global methods solve all nodes simultaneously and jointly. This ensures a kinematically compatible deformation field, but the process is generally more computationally demanding [43].

2.6.1 TomoWarp2

TomoWarp2 is a custom-built, open-source DVC software developed collaboratively by Lund University and the University Grenoble Alpes, France [45]. It originated from TomoWarp, initially crafted for analyzing 4D seismic images and later adapted for 4D X-ray

tomography of deforming materials. With its roots in geomechanics, TomoWarp2 explores localized deformations in geomaterials and has diversified its applications to include research on battery processes and bone-implant interfaces [46].

The Tomowarp2 software forms a local DVC method which besides two 3D images takes as input three tuples that define the x, y, and z values in pixels for a correlation window (CW), a search range window (SW), and the node space (NS). For each node, all subvolumes within the SW in the deformed image are correlated with the nodal subset in the reference image and the maximum value is returned. This represents arguably the most direct approach to solving Equation 2.1. Nevertheless, an option to carry out subpixel optimization is available, offering two different alternatives. The fastest method (correlation coefficient refinement) involves finding the maximum of a function that interpolates the correlation coefficient at 27 points surrounding the best integer-displacement match. The second method (image interpolator translation) numerically displaces the subset of the deformed image until it matches the reference one. Possible optimization procedures for this alternative include Powell's conjugate direction method and the BFGS algorithm.

Tomowarp2 uses SIMD parallelisation for the synchronization of subset computations and the pixel search has been written in C for quickening data processing. The structure of the program is profoundly modular and comprises three main concurrent processes. The `DIC_setup` calculates the required data extents for the images and communicates this global extent information to the `data_delivery_worker`, which handles data loading and data communication. Specifics about nodes and their extents are placed into a global job queue for reading by the `DIC_worker`(s), which are a number of identical processes performing the point-by-point correlation [46].

2.6.2 ALDVC

ALDVC (Augmented Lagrangian DVC), is a 3D extension of the ALDIC (Augmented Lagrangian Digital Image Correlation) algorithm and originates from the University of Wisconsin-Madison, USA. It represents a relatively recent addition to the field of DVC (2020) and was developed to overcome the limitations of both local and global DVC methods by constructing a hybrid algorithm that incorporates features from both approaches [43]. The ALDVC software is open-source and has been used to explore the internal strain behavior of Carbon-Aramid hybrid braided composites, for instance [47].

In order to explain the ALDVC method, subset displacements $\mathbf{u}_i$ and deformation gradients $\mathbf{F}_i$ are introduced, and likewise a global kinematic compatibility constraint $\mathbf{F} = \mathbf{Du}$. $\mathbf{D}$ is an appropriate discrete gradient operator, and for efficient handling of the constraint, the incorporation of an auxiliary compatible global displacement field, $\hat{\mathbf{u}}$ is made. It is set to satisfy

$$\mathbf{F}_i = \nabla \hat{\mathbf{u}}_i(\mathbf{X}_{i0}), \mathbf{u}_i = \hat{\mathbf{u}}(\mathbf{X}_{i0}), \tag{2.4}$$

where $\mathbf{X}_{i0}$ represents the center point of the local subset Ω_i. The augmented Lagrangian method is then applied to the expression in (2.3). The AL method creates an unconstrained problem from an originally constrained dito by having the objective function minimized as

$$\Phi_k(\mathbf{x}) = f(\mathbf{x}) + \frac{\mu_k}{2} \sum_I c_i(\mathbf{x})^2 + \sum_i \lambda_i c_i(\mathbf{x}), \tag{2.5}$$

where λ_k is increased for every step k in a manner akin to the penalty method, and the solution for step $k-1$ is used as initialization. Further is f the original objective function, $c_i = 0$ its constraint, and I is the index set for these equality constraints, $i \in I$. λ_i are additionally updated for each k as $\lambda_i \leftarrow \lambda_i + \mu_k c_i(\mathbf{x}_k)$ [43], [48].

Back to the ALDVC formulation, the deformation mapping y can be written as $\mathbf{y}(\mathbf{X}) = \mathbf{X}_i + \mathbf{u}_i + \mathbf{F}_i(\mathbf{X} - \mathbf{X}_{i0})$, which inserted in (2.3) and by applying the AL formulation gives the functional

$$
\begin{aligned}
\mathcal{L}_0 = \sum_i \int_{\Omega_i} \bigg(& |f(\mathbf{X}) - g(\mathbf{X} + \mathbf{u}_i + \mathbf{F}_i(\mathbf{X} - \mathbf{X}_{i0}))|^2 \\
& + \frac{\mu_1}{2}|(\mathbf{D}\hat{\mathbf{u}})_i - \mathbf{F}_i|^2 + \boldsymbol{\lambda}_{1i} \vdots ((\mathbf{D}\hat{\mathbf{u}})_i - \mathbf{F}_i) + \frac{\mu_2}{2}|\hat{\mathbf{u}}_i - \mathbf{u}_i|^2 + \boldsymbol{\lambda}_{2i} \cdot (\hat{\mathbf{u}}_i - \mathbf{u}_i) \bigg) d\mathbf{X}
\end{aligned}
\tag{2.6}
$$

with Lagrange multipliers $\boldsymbol{\lambda}_i$. For matrices, the Frobenius norm is used while the L2-norm is used for vectors. $\vdots$ represents the double dot product between matrices, $\mathbf{A}\vdots\mathbf{B} = \sum_i \sum_j A_{ij}B_{ij}$. By setting $\mathbf{W}_i := \boldsymbol{\lambda}_{1i}/\mu_1$ and $\mathbf{v}_i := \boldsymbol{\lambda}_{2i}/\mu_2$, (2.6) becomes simplified to

$$
\begin{aligned}
\mathcal{L}_0 = \sum_i \int_{\Omega_i} \bigg(& |f(\mathbf{X}) - g(\mathbf{X} + \mathbf{u}_i + \mathbf{F}_i(\mathbf{X} - \mathbf{X}_{i0}))|^2 \\
& + \frac{\mu_1}{2}|(\mathbf{D}\hat{\mathbf{u}})_i - \mathbf{F}_i + \mathbf{W}_i|^2 + \frac{\mu_2}{2}|\hat{\mathbf{u}}_i - \mathbf{u}_i + \mathbf{v}_i|^2 \bigg) d\mathbf{X}.
\end{aligned}
\tag{2.7}
$$

To minimize this functional with respect to our primal variables $\{\mathbf{u}_i^k\}, \{\mathbf{F}_i^k\}, \{\hat{\mathbf{u}}_i^k\}$ and duals $\{\mathbf{W}_i^k\}, \{\mathbf{v}_i^k\}$, the Alternating direction method of multipliers (ADMM) is employed. The ADMM is a modification of the augmented Lagrangian method in which the minimization process is divided into two steps where in the first one the primal variables are the subject of minimization and then, in the next step, a dual variable update is performed [49]. The iteration between these steps is possible because of the separability in these variables, and the process prompts the convergence to an approximate solution under certain assumptions.

The primal optimization search is subdivided into two steps, subproblems 1 and 2. In subproblem 1 the local displacement update is made, which can be fulfilled independently since $\{\hat{\mathbf{u}}_i^k\}$ is known:

$$
\begin{aligned}
\mathbf{u}_i^{k+1}, \mathbf{F}_i^{k+1} = \arg\min_{\mathbf{u}_i, \mathbf{F}_i} \int_{\Omega_i} \bigg(& |f(\mathbf{X}) - g(\mathbf{X} + \mathbf{u}_i + \mathbf{F}_i(\mathbf{X} - \mathbf{X}_{i0}))|^2 \\
& + \frac{\mu_1}{2}|((\mathbf{D}\hat{\mathbf{u}})_i^k - \mathbf{F}_i + \mathbf{W}_i^k|^2 + \frac{\mu_2}{2}|\hat{\mathbf{u}}_i^k - \mathbf{u}_i + \mathbf{v}_i^k|^2 \bigg) d\mathbf{X}.
\end{aligned}
\tag{2.8}
$$

However, a simplification is made to improve speed and accuracy, by setting $\mathbf{F}_i^{k+1} = \mathbf{D}\hat{\mathbf{u}}_i^k$ and solve for $\mathbf{u}_i^{k+1}$ only. This is accomplished with the ICGN (Inverse Compositional Gauss-Newton) method which is described in [43]. In the subsequent subproblem 2, the global update is executed by minimizing with respect to the auxiliary global field $\hat{\mathbf{u}}$, a problem that is independent of images f and g:

$$\{\hat{\mathbf{u}}_i^{k+1}\} = \underset{\hat{\mathbf{u}}_i}{\arg\min} \sum_i \int_{\Omega_i} \left(+\frac{\mu_1}{2}|(\mathbf{D}\hat{\mathbf{u}})_i - \mathbf{F}_i^{k+1} + \mathbf{W}_i^k|^2 + \frac{\mu_2}{2}|\hat{\mathbf{u}}_i - \mathbf{u}_i^{k+1} + \mathbf{v}_i^k|^2 \right) d\mathbf{X}.$$

(2.9)

This can be reduced to a linear problem:

$$\hat{\mathbf{u}}^{k+1} = \left(\mu_1 \mathbf{D}^T \mathbf{D} + \mu_2 \mathbf{I} \right)^{-1} \left(\mu_1 \mathbf{D}^T \mathbf{a} + \mu_2 \mathbf{b} \right),$$

(2.10)

where $\mathbf{a} = \{\mathbf{F}_i^{k+1} - \mathbf{W}_i^k\}$ and $\mathbf{b} = \{\mathbf{u}_i^{k+1} - \mathbf{v}_i^k\}$: Since we have μ_1 and μ_2 fixed, this is a simple matrix-vector multiplication and the sparse, diagonal-like nature of $\mathbf{D}$ permits for efficient computation. In subproblem 3 the dual variables are finally updated:

$$\mathbf{W}_i^{k+1} = \mathbf{W}_i^k + \left((\mathbf{D}\hat{\mathbf{u}})_i^{k+1} - \mathbf{F}_i^{k+1} \right),$$

(2.11)

$$\mathbf{v}_i^{k+1} = \mathbf{v}_i^k + \left(\hat{\mathbf{u}}_i^{k+1} - \mathbf{u}_i^{k+1} \right),$$

(2.12)

The three subproblems of ADMM are iterated and under some assumptions on convexity and saddle points there will be asymptotical convergence,

$$(\mathbf{D}\hat{\mathbf{u}}^k - \mathbf{F}^k) \to \mathbf{0},$$

(2.13)

$$(\hat{\mathbf{u}}^k - \mathbf{u}^k) \to \mathbf{0},$$

(2.14)

$$(\hat{\mathbf{u}}^{k+1} - \hat{\mathbf{u}}^k) \to \mathbf{0},$$

(2.15)

as $k \to \infty$.

Similar to TomoWarp2, the ALDVC method uses a correlation window and node spacing specified by pixel values in three Cartesian directions (x, y, z). Depending on the choice of the initial guess method, a search range may also be required. There are five initial methods based on whether prior information about the displacement field is available or not, and in such cases whether displacements are considered small or large. The methods offered are zero normalized cross correlation and phase cross correlation, and they do both have specializations for small and large deformations. If the alternative of no prior information is chosen, a multiscale zero normalized cross correlation based on an image pyramid is performed. Besides, it is possible to choose between employing the finite difference method or the finite element method for the global step, and to utilize parallel computing with Matlab parallel pools. A parallel pool is a collection of Matlab workers where each worker operates independently and can execute Matlab code [50]. By distributing tasks across multiple processors or cores the local search of the optimization procedure can be accelerated. In ALDVC, strains can be obtained as the direct output of the deformation gradient minus identity, $\mathbf{F}$. Three other methods can be used to compute strains from the solved displacements, including the central finite difference method and a plane fitting method [51].

Chapter 3

Material and methods

3.1 Material

The sample preparation and in situ loading during time resolved tomography described at 3.1.1-3.1.2 below were executed before the start of this project.

3.1.1 Samples

Two samples of human medial menisci from the MENIX biobank at Skåne University Hospital in Lund and one bovine medial meniscus sample were used. The human donors were deceased at an age of 84, and one of them showed signs of possible degeneration while the other appeared intact and healthy. The bovine meniscus showed no visible signs of disease. From the samples cylindrical plugs of 4mm in diameter were extracted. To facilitate referencing throughout the text, each sample is designated with a name corresponding to Table 3.1.

Bovine	Human (healthy)	Human (degenerated)
0	1	2

Table 3.1: Sample names used in the report.

3.1.2 In-situ loading and time-resolved synchrotron-based phase-contrast computed tomography

3D images of the samples were taken at the TOMCAT beamline (Paul Scherrer institute, Switzerland) by phase contrast enhanced x-ray μCT tomography. A rheometer setup was used for mechanical loading (Figure 3.1). The plugs were inserted into a specially designed 3D-printed holder filled with saline solution to maintain sample hydration. Either 40 second (4000 projections and 9ms exposure time) or a 5 second scans (2000 projections and 2.5ms exposure time) were taken. An x-ray energy level of 21 keV was used and the distance between the sample and detector was 40 cm. The bovine sample (sample 0) was imaged four times in static conditions. Two scans of 40s and 5s were conducted, followed by sample removal and replacement on the stage. Two additional scans were then performed, again with
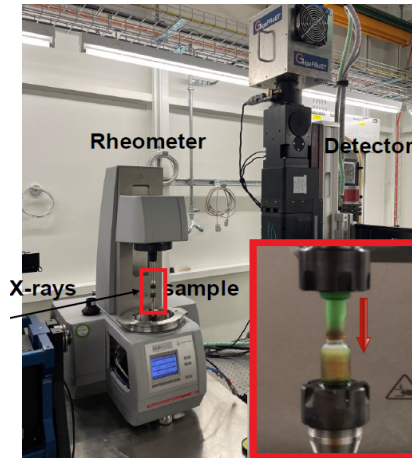
Figure 3.1: Setup for in situ loading in TOMCAT.

40s and 5s durations. The human samples (sample 1 and 2) were tested in a stress-relaxation protocol. Static scans of 40s were implemented before and after the mechanical protocol. A piston was used for compression, and a preload of 2 N was initially applied. The preload was used to establish proper contact between the piston and the sample. Two steps of 15% and 30% strain, respectively, were applied at 1% strain per second in the course of 15 seconds. After the first load there was a relaxation period of 600s and after the second load the relaxation time was 900s. Tomographic volumes (5 second scans) were obtained just before each load step and at intervals during relaxation, with a total of 15 scans per sample (Table 3.2 and Figure 3.2). Volume reconstruction was performed using the Gridrec algorithm [52], followed by the Paganin retrieval method [53]. The field of view was 2016×2016 pixels and the pixel size was 2.75 μm. Image stacks were in all cases of length 1400. This experiment was carried out in 2022, which predates the start of this project. The volumes have thus been available from the beginning of the project and the author's work enters here.

Step	1	2	3	4	5	6	7	
Retrieval time (s)	0	20	40	60	100	300	600	
Step	8	9	10	11	12	13	14	15
Retrieval time (s)	0	20	40	60	100	300	600	900

Table 3.2: The time points after which an image acquisition was made in the stress-relaxation test. The upper rows show times relative to the first compression step and the lower rows show times that are relative to the second compression.

3.1.3 Hardware and software

All mathematical processing was conducted on a computer equipped with an Intel i7-9800X processor, having a base clock of 3.50GHz (8 threads), 64GB memory, and was operated on
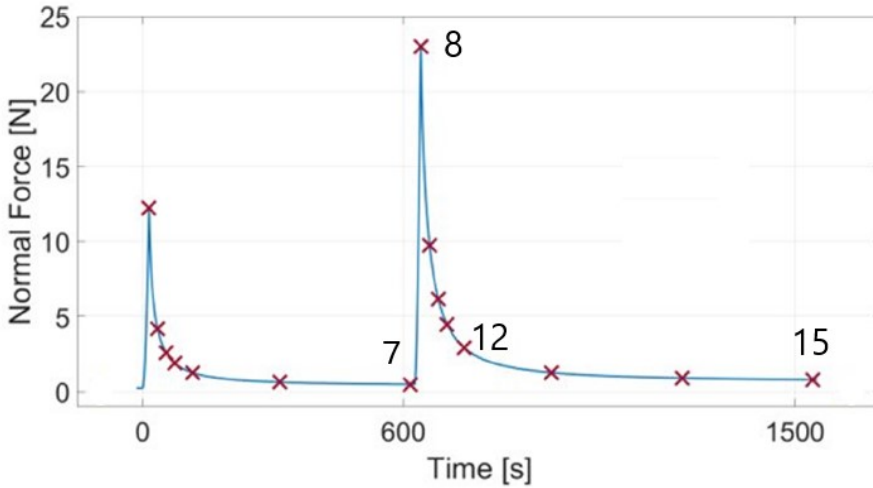
Figure 3.2: The applied force as a function of time, resulting from the test. Crosses mark the time points when 5s imaging was made, and those that are most relevant for the project are numbered.

a Windows 10 platform. 4 threads were used with the parallel processing toolbox in Matlab, as well as with Python multiprocessing libraries. Digital volume correlation was made in Matlab 2023a and Python 2.7.16. Moreover, ImageJ 1.54d was used for image visualization and manipulation [54].

3.2 Methods

The project was executed in two stages, one analyzing volumes of static tissue in a zero-strain study, and the second analyzing dynamic sample volumes to calculate actual strains. Two DVC programs were used, Tomowarp2 and ALDVC, which were described in the background chapter. The analysis of the static volumes was done to evaluate sources of error and to define the parameters for the algorithm to use in the next phase, the analysis of the dynamic data. The performance of the two algorithms was compared and, based on criteria like accuracy, precision, and node error frequency, the most suitable algorithm was chosen for the dynamic stage. Further parameter optimization was performed for this algorithm in the second phase in order to enhance the accuracy and reliability of displacement and strain measurements derived from the volumetric image data.

3.2.1 Analysis of the static volumes

Conditions of the four scans used in the analysis are indicated in Table 3.3. Scan 3 and 4 were registered against scan 1 and 2. This was done in Matlab in two steps. First, a linear geometric transformation was fit between the top slices from scan 3 and 1, by having the scan 1 volume as the reference object. This transformation was then applied to all slices in volume 3 and 4. The zero-strain DVC tests were made between scans 1 and 2, 3, 4,

respectively. A major focus was on the correlation between 1 and 4. The reason was that it would set an approximate upper limit of the noise levels, regardless of whether a 40s scan would be included later in the project.

Scan	**1**	**2**	**3**	**4**
Duration (s)	40	5	40	5
Before/After	Before	Before	After	After

Table 3.3: Exposure time for the static meniscus volumes, and whether the scan was made before or after repositioning.

Tomowarp2

A sub-volume of interest (VOI) extending from top to bottom of the sample was selected from the original volumetric data to contain as few artifacts as possible (longitudinal size: 960 pixels). The shape of the cross-section area selected was chosen for simplicity to be square and the size of 200×200 pixel^2 as a compromise between a large field-of-view and computation time. The position of the chosen subvolume within the 4mm diameter sample can be seen in Figure 3.3.
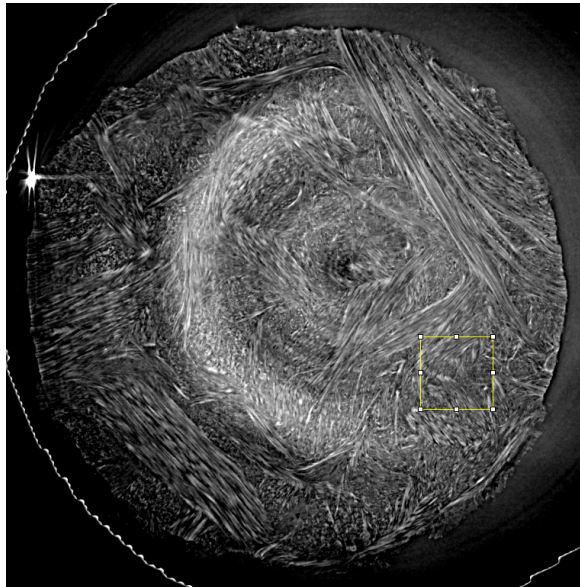

Figure 3.3: The yellow square highlights the chosen region of size 200×200 pixels for which the zero strain analysis was performed. Ring artefacts concentrated to the middle region were avoided.

The shapes of the correlation window (CW) and the search window (SW) were chosen to

be cubic due to the absence of expected significant deformations in any specific direction. The distribution of small, high-contrast details within the volumes intended for tracking forms what is commonly referred to as a speckle pattern. A CW of side 24 pixels, $s_{cw} = 24$ was by visual inspection regarded to be a minimal size containing the necessary $3 \times 3 \times 3$ speckles for achieving a sufficient accuracy in window matching [55]. Figure 3.4 shows its range. Some attempts with CW volumes of this magnitude and above were made to determine a rough search window upper bound, based on the maximum expected displacement. The obtained displacement values prompted the decision that a 40% relation between the CW and SW sides should be the minimum in further tests, i.e. $s_{cw} \geq 0.4 \cdot s_{sw}$. A node spacing d_{ns} equal to $s_{sw}/2$ was used since this was considered a fair compromise between spatial resolution and computational efficiency when doing a larger number of tests.
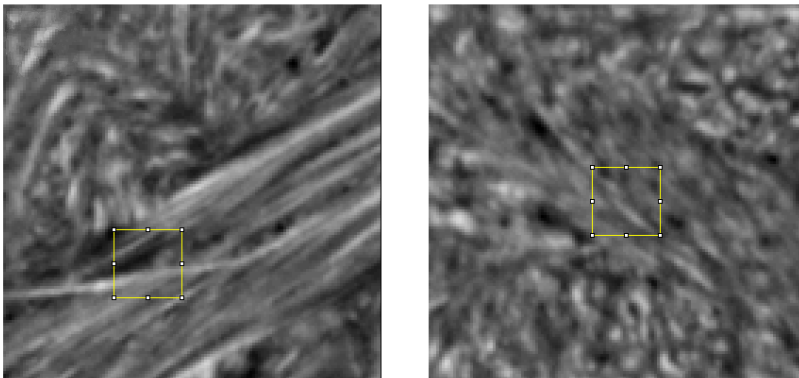

Figure 3.4: The minimal correlation window used in strain-free assessments, relative to the speckle pattern. The left image shows a VOI slice in the XY-plane and the right shows part of a slice in the XZ-plane. The CW is marked in yellow.

A combination of grid searching and a trial-and-error approach was followed in accordance with the set parameter limitations. Three different window size ratios were included in the analysis, $\frac{s_{cw}}{s_{sw}} \in \{0.4, 0.5, 0.75\}$. The range of s_{sw} that was used was $[32, 100]$ pixels, and consequently was the NS range $d_{ns} \in [16, 50]$. CW sizes spanned in the interval $s_{cw} \in [24, 54]$. DVC was done in either one or two rounds. In the first run the correlation coefficient subpixel optimization was utilized, and in a second run the mode for subpixel optimization was image interpolator translation (see 2.6.1). In the second round, the DVC process was run only for nodes in which an error had occurred.

A mask to consider only fiber within the tissue was applied to the volume to examine the effect on accuracy and node error ratio upon application. The mask was created using Otsu's method, following which the output threshold value was fine-tuned based on visual observation, to determine the final binary mask to precisely select only fibers. The outcome is visible in Figure 3.5.
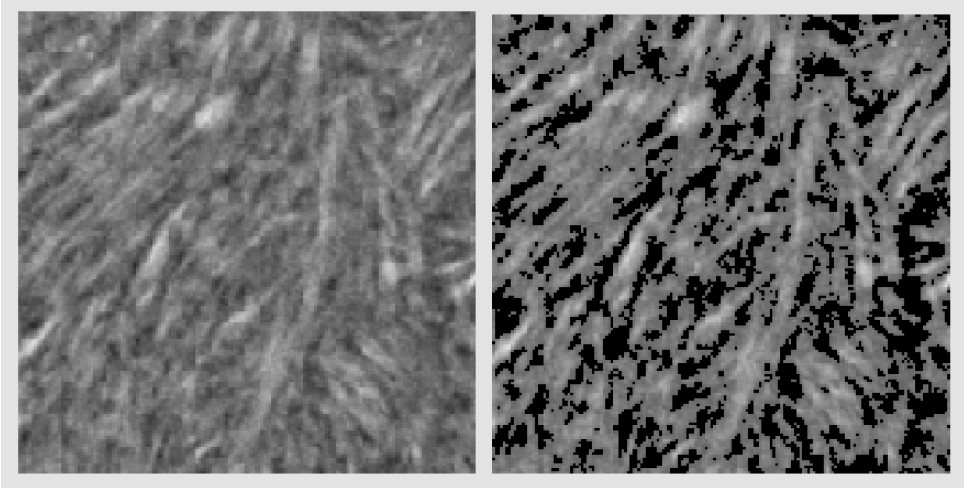
Figure 3.5: A slice of the VOI before and after the masking operation.

ALDVC

The same sub-volume of interest (VOI) with dimensions $200 \times 200 \times 960$ voxels, previously utilized in Tomowarp, was again considered for the analysis in ALDVC. Parameters that the two methods have in common are correlation window size and node distance. ALDVC does not explicitly require a defined search window by the user since it instead implements a constrained numerical optimization search. Guidelines are provided for parameter selection in the algorithm. The correlation window side is preferably set between 10-30 pixels, and the node space should be approximately 0.25-1 times this size. At least 3-5 features should be included in the window. The zero-strain analysis in ALDVC did therefore generally involve smaller window and node space inputs compared to Tomowarp. However, the recommended upper limit for the correlation window size was extended to align with the Tomowarp experiments. The tested range for this parameter was $s_{cw} \in [20, 50]$, which conveniently met the feature inclusion criterion. A grid search with node spaces of $d_{ns} \in \{0.25, 0.5, \frac{2}{3}, 0.75, 1\} \cdot s_{cw}$ was implemented. As initial guess method the multi-scale, zero normalized cross-correlation was used. Infinitesimal strains were derived from the calculated displacement field using the finite difference method, consistent with the methodology applied in the global ADMM step [51].

For both DVC programs, a couple of trials were conducted on identical volumes with different locations within the meniscus to assess result consistency. Furthermore, larger volumes were utilized to investigate time complexity and variations in metrics such as accuracy and node error proportion. A comparative examination of the two algorithms was performed to guide the subsequent dynamic DVC scrutiny. Key metrics, including accuracy, precision, computation time, and the number of failed nodes, were taken into account. Accuracy and precision were evaluated using the root-mean-square error (RMSE), between the calculated

strain values and the true values of 0.

3.2.2   Analysis of the dynamic volumes

ALDVC was considered the more suitable method for the phase involving compressed meniscus volumes, and Tomowarp was excluded from this assessment. Execution of DVC was made for volumes of samples 1 and 2 in Table 3.1. Computations were done cumulatively, with volumes from two time steps (7 and 8) as references, and deformed volumes from three following time points (8,12, and 15). Acquisition times for the steps are listed in Table 3.2 and all the combinations that were correlated are displayed in Table 3.4. All image stacks were padded with 70 images at the end, with the same 2016×2016 pixel size as the original ones. The purpose of the padding was to offset the impact of the software cropping mechanism, which, without this adjustment, would have excluded a significant number of images containing the meniscus sample. Figure 3.6 shows image slices from the first volume pair.
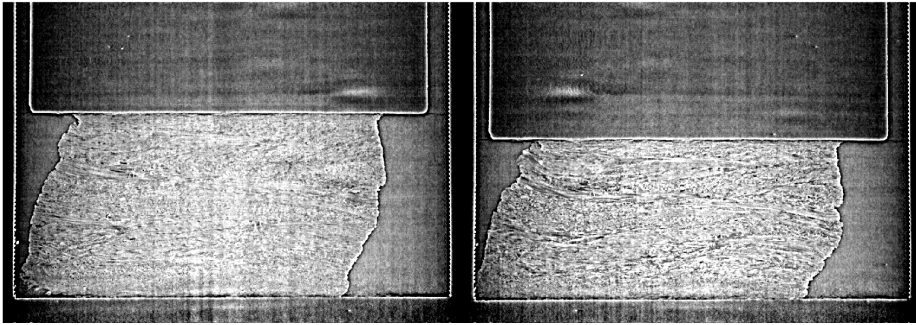

Figure 3.6: Two image slices from an internal part of a meniscus during stress-relaxation. The time instances are 7 (left) and 8 (right).

The first pair of volumes to perform DVC on were 7 and 8, and most of the experiments were conducted for this pair. Volumes of interest were selected to be quadratic cuboids, extending vertically from the top to the bottom of the sample, similar to the static case. In this case the volumes were larger, with cross-sectional dimensions ranging from 400^2 to 900^2 pixels. Additionally, a pixel binning approach was tested to mitigate noise and reduce computational time. This was done by averaging every $2 \times 2 \times 2$ adjacent voxels to create a new volumetric image. Since this implies a $\frac{7}{8}$ volume reduction, substantially larger regions of the meniscus sample could be explored within an equivalent time frame. Volumes subject to voxel binning had cross-sectional areas of $1000^2 - 1500^2$ pixels, with the upper limit incorporating almost the entire sample. For the binned volumes, a conversion from double to single precision was made to ease the memory load. A similar conversion of the original volumes was not feasible since their values were of the smallest possible data type (uint8). Another strategy to reduce computational burden was to input cropped regions, at most marginally larger than the current VOI, rather than the entire volumes into the algorithm.

To determine an initial displacement field, a zero normalized cross-correlation for large de-

formation was used. It is important to provide this function with a search zone that is larger than the maximum displacement in any direction. The zone extension was determined by first measuring in ImageJ to get a rough estimate, and then run tests where this value was tuned depending on the resulting node convergence rates. While this was the first parameter to undergo optimization, other parameters such as CW size (s_{cw}), NS distance (d_{ns}), and the maximum number of the inner loop (ICGN) respectively outer loop (ADMM) iterations were maintained at relatively constant values. The ICGN and ADMM threshold values were fixed at 0.01. After establishing the initial search zone, the focus shifted to optimizing CW size and NS distance. Keeping NS distance at a constant percentage of CW size, a line search was made within and slightly outside the recommended limits. By studying the node convergence rates, a value for s_{cw} was fixed and tuning of d_{ns} was performed. Once this parameter was finalized, the optimization of iteration numbers commenced. A grid search was carried out for these two variables. For both meniscus samples a parameter tuple was settled for the first volume pair. Subsequently, DVC computations were performed using this tuple as input for the other three combinations of volumes.

Ref / Def	8	12	15
7	X		X
8		X	X

Table 3.4: Combinations of reference and deformed volumes for which DVC was carried out with ALDVC, marked with an X.

Chapter 4

Results

4.1 Zero strain DVC

Given that a predominant portion of the simulations in this part of the project focused on the analysis of volumes 1 and 4, the results presented in this section pertain specifically to this volume pair unless stated otherwise.

4.1.1 Tomowarp

The Tomowarp program was run with three window size ratios, $s_{cw}/s_{sw} \in \{0.40, 0.50, 0.75\}$. Table 4.1 shows the results for attempts with each of them. A node is regarded as failed if it encountered an error during the Tomowarp computations. Out of the three ratios, the largest had an evidently lower node failure percentage and the lowest root-mean-square error (RMSE) averaged over the different tests. Windows with this side proportion were used to a higher extent since this pattern was early discovered. Particularly was a number ($\sim$10) of second runs for failed nodes made with a parameter combination resulting from a side ratio of 0.75 as the base. This was made with the image interpolation subpixel mode which is described in 2.6.1, and in Table 4.2 are the results for one such recalculation. The mean computation time for the single-run tests was 78 min.

Table 4.1: Zero strain tests with Tomowarp, from repeated scans (volumes 1, 3, and 4 in Table 3.3). For each window size ratio, the mean values (and standard deviations) are presented for node failure (NF) rates and the RMSE of the strains. N is the number of tests for each window ratio and volume combination.

$\frac{s_{cw}}{s_{sw}}$	**1 & 3**	NF (%)	RMSE (10^{-4})	N	**1 & 4**	NF (%)	RMSE (10^{-4})	N
0.4		66 (9)	127 (23)	6		69 (14)	227 (89)	6
0.5		65 (8)	124 (32)	5		65 (7)	198 (44)	5
0.75		49 (9)	117 (17)	5		55 (4)	151 (23)	14

The program struggled to provide displacement values in some areas of the volume where pronounced artifacts can be spotted, which is reflected in high node failure rates in

Table 4.1. For all simulations, the lowest failure rate was 0.46. This was the case for the tuple considered in Table 4.2, and was achieved for both rigid body transformations (scan 1 against 3 and 4). It also had the lowest RMSE for all tests. The second runs in this case could supply values for extensively more nodes, by decreasing window sizes, but the RMSE witnessed a sharp upswing.

Table 4.2: Parameters and statistics for a two-stage computation. The first round was made with correlation coefficient interpolation and the second was made with image interpolation for all failed nodes from the first round. The RMSE values are for all non-failed nodes.

round	s_{sw}	d_{ns}	s_{cw}	node failure (%)	RMSE (10^{-4})
1	64	32	48	46	116
2	28	32	20	6	172

We tested a masking procedure focusing solely on fibers within the volumes to investigate reduction possibilities of node and strain errors. Masked volumes obtained from masks with threshold values of 0.37, 0.41 and 0.45 were constructed. The middle value was chosen as a minor deviation of the output from Otsu's method, and the other two were tried afterwards since the first attempt was considered unsuccessful. The appliance of masks did not reduce errors but rather escalate them. For $s_{cw} = 32, s_{sw} = 80, d_{ns} = 40$, the RMSE were 0.138, 0.110 and 0.0681, as compared to 0.0164 in the non-masked case.

4.1.2 ALDVC

The static DVC computations of zero-strain for ALDVC are addressed next. This algorithm provided values for all nodes but some of them did not converge for the chosen values of thresholds and maximum iteration numbers (the information is available in the cell array named 'ResultConvItPerEle'), and are therefore less reliable. They are denoted as failed nodes which makes a fairly reasonable comparison possible between the two methods. The upper iteration limit for the inner loop was set to 100, while the outer loop limit was set to 4, and increasing these values did not improve convergence remarkably. Table 4.3 shows ALDVC processing for two values of s_{cw} and varying d_{ns}. Widening of the node spacing lowers the RMSE, trading off for lower resolution and raised node failure percentage. Most of the nodes that fail, i.e. do not converge, are at the boundaries of the volume. The larger node space, the larger is the share of nodes that are part of the boundary, which could explain the node failure increase. The average computation time for all tests was 33 min.

Table 4.3: ALDVC zero strain outcome for two window sizes.

s_{cw}/d_{ns}	RMSE (10^{-4})	node failure (%)	time (min)
24/6	164	12	155
24/12	134	17.1	19
24/16	131	15.3	12
24/24	101	27.4	3
30/8	155	12.4	85
30/15	138	12.9	21
30/20	112	22.7	8
30/30	102	20.7	6

4.1.3   Comparison between Tomowarp and ALDVC

A subset of input combinations is further used in a comparative analysis between Tomowarp and ALDVC for static volumes (Table 4.4). ALDVC is configured for 1000 inner iterations, compared to the standard tests with 100 iterations in the previous section. As apparent from the results, ALDVC provides higher accuracy and precision in all instances with on average 41% lower RMSE, discarding the extreme value for Tomowarp. The node error rates are notably lower in ALDVC calculations, and the elapsed time is consistently lower throughout the tests. The superior computational efficiency of ALDVC is particularly evident for the sparser node spacing distances.

Table 4.4: Comparison of the two algorithms in regards of accuracy & precision (RMSE), node failure (NF) rates and computation time (t). The RMSE values are for the non-failed nodes.

s_{cw}/d_{ns}	ALDVC			Tomowarp		
	RMSE (10^{-4})	NF (%)	t (min)	RMSE (10^{-4})	NF (%)	t (min)
24/16	136	13	24	196	49	34
30/20	113	22	12	162	51	59
36/24	113	17	9	162	57	85
42/28	105	19	6	167	57	135
48/32	89	22	7	116	46	186
24/24	101	26	7	212	62	31
30/30	123	20	7	135	68	41
36/36	118	23	4	16244	74	65

A fixed parameter tuple was employed in each of the algorithms for a couple of larger VOI:s of growing size, which are visible in Figure 4.1. All VOIs extend from top to bottom of the sample, and are increasing $2.6 - 2.8$ times per step. Table 4.5 illustrates the metric variation in this respect. Concerning accuracy, there is a somewhat descending trend in both cases, although a bit stronger for Tomowarp. Both algorithms show linearly increasing be-

23

haviour in time consumption as the volume grows, but for Tomowarp the rise is undeniably more enhanced. The occurrence of node failures declines to some extent for both methods, but it remains relatively high across all experiments in Tomowarp. Figure 4.2 highlights the algorithm's difficulties with transversal fibers and, to some extent, ring artifacts. The intensity variance is generally lower in these areas.
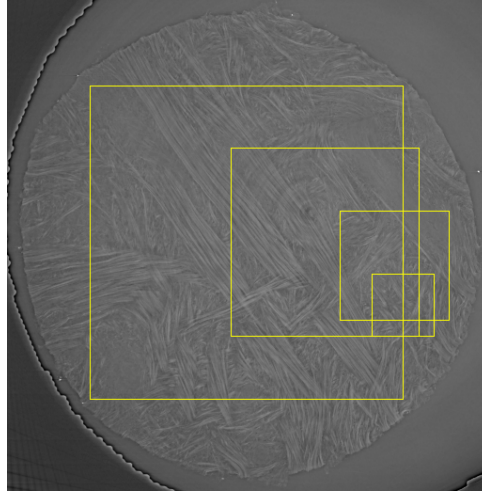

Figure 4.1: Cross-section squares for the VOI:s of different sizes for which a fixed parameter combination was evaluated. The volumes extend from top to bottom of the sample.

Table 4.5: Key metric variation for different volumes. The RMSE values are for the nodes that were not considered failed.

ALDVC ($s_{cw} = 24, d_{ns} = 24$)			
volume (10^6 voxels)	RMSE (10^{-4})	node failure (%)	time (min)
38	101	27	5
104	131	13	20
292	138	10	83

Tomowarp ($s_{cw} = 24, d_{ns} = 30$)			
volume (10^6 voxels)	RMSE (10^{-4})	node failure (%)	time (min)
38	162	72	24
104	297	57	90
292	460	61	241
578	274	60	622
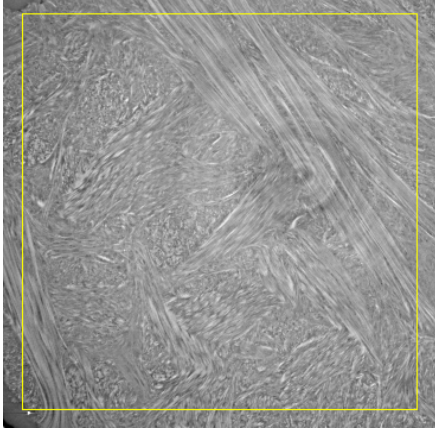
(a) Cross section of the largest test volume, in slice 660, which is just over a quarter into the VOI. Its borders are marked in yellow. The contrast has been adjusted to highlight fibers and ring artifacts.
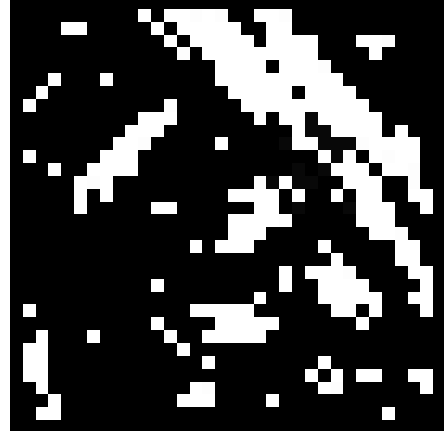

(b) Error field in Tomowarp displacement computations for the area within the yellow VOI border. A white pixel signifies that an error occurred in this node.
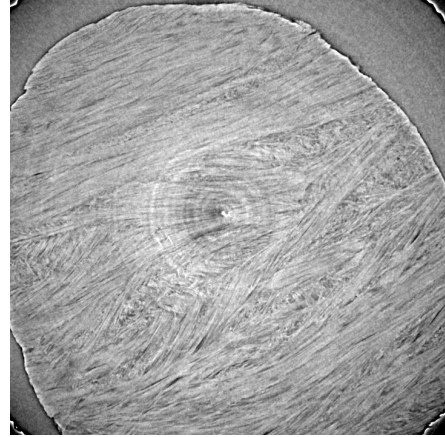
Figure 4.2: Tomowarp displacement errors for the largest VOI. Some correlation between transversal fibers and node errors can be observed.

4.2 Dynamic DVC

The method used for dynamic DVC was ALDVC, and the corresponding outcomes are presented here. Volumes that were subject to correlation in this phase were scans 7, 8, 12, and 15 of meniscus 1 & 2 (see Method section). Both the originals and $2 \times 2 \times 2$ average pixel binned equivalents were tried, and Figure 4.3 shows the effect of binning. The binned volumes had higher convergence rates compared to the original volumes, prompting their selection for the final DVC processing. Additionally, the binned volumes offered increased flexibility for parameter adjustments due to their shorter calculation times. The ultimate volume choice settled on a $1440 \times 1440 \times 1110$ voxel volume for the healthy meniscus and a $1440 \times 1440 \times 790$ voxel volume for the degenerated meniscus, where the third dimension represents the whole height of the samples which was greater in the case of the healthy sample. Consequently, the binned volumes had dimensions of $720 \times 720 \times 555$ and $720 \times 720 \times 395$ voxels, respectively. Parameters that were used in the final computations are listed in Table 4.6.
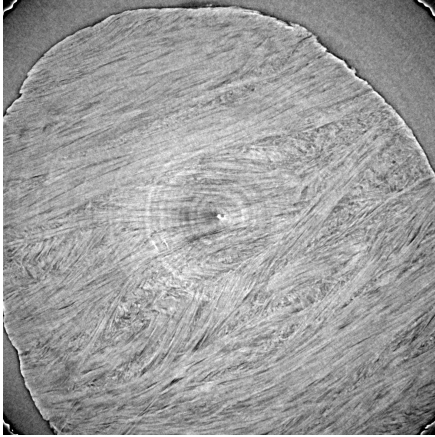
(a) Lateral cross-section in the original vol- (b) Cross-section in the pixel-binned volume,
ume.   corresponding to the one in (a).

Figure 4.3: Comparison between unbinned and binned images.

Table 4.6: The final parameter settings for dynamic ALDVC. The three first values are in pixels.

initial search zone	s_{cw}	d_{ns}	$N_{max.iter.}$ (inner loop)	$N_{max.iter.}$ (outer loop)
70	30	30	5000	7

Volume 7 and 8 for meniscus 1 can be observed in Figure 4.4 and displacements for the conclusive correlation between these are shown in Figure 4.5. The longitudinal displacement in the z-direction reaches its maximum value of around 0.314 mm at the compression area and gradually decreases towards a minimum of 0.066 down the sample, in the positive z-direction. The maximum recorded displacement along z is consistent with the fact that the initial sample height was 2.1 mm, and the applied deformation was 15%. The magnitudes for displacements in the x- and y-directions are significantly lower on average, with mean absolute values of 0.0420 mm and 0.0956 mm, compared to 0.223 for z-displacements. There is a tilt in the equilibrium line for displacements in the transversal directions (Figure 4.6). Given the slanted surface of the sample and the potential for non-uniform application of compression, this observation may be anticipated.
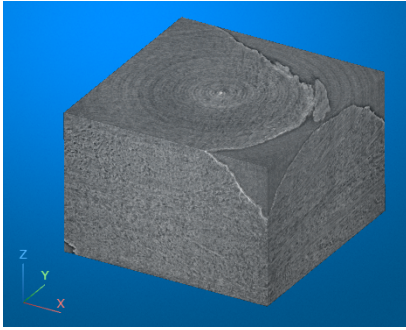
26

(a) State of the sample at time instance 7, immediately before stress imposure. Some air space can be seen in a darker gray color at the edges.
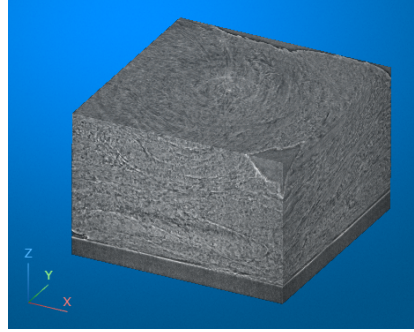
(b) The sample state immediately after stress imposure, time instance 8. Similar to volume 7, a few ring artifacts are noticeable at the top.

Figure 4.4: Volumes 7 and 8 from meniscus 1, which was the first pair to be correlated. A portion of the piston is visible at the bottom of volume 8, which means that the pressure is applied from below. Note that this is the reverse of the direction observed in the experiment.
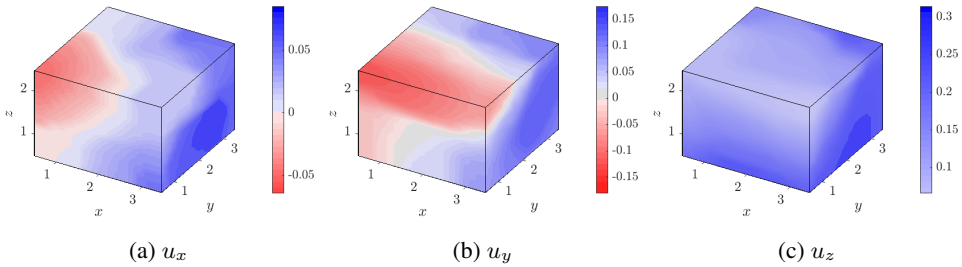

(a) u_x

(b) u_y

(c) u_z

Figure 4.5: Displacements for meniscus 1, between time step 7 and 8. All measurements are in mm. The compression is applied in positive z-direction.
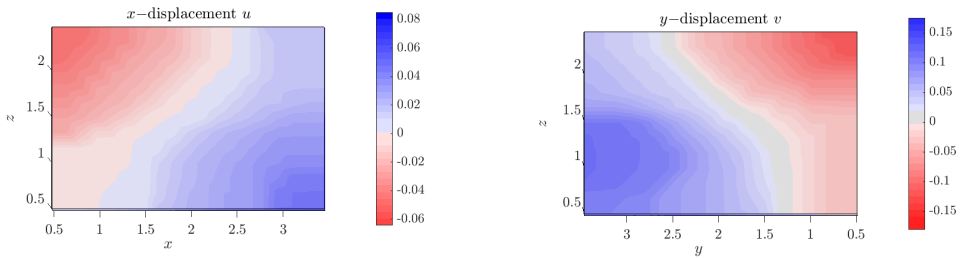

(a) Slant in x-displacement field from the first y-slice.

(b) Slant in y-displacement field from the first x-slice.

Figure 4.6: Slants in transversal displacement fields due to the uneven surface preassure. The measurements are in mm.

The calculated displacement fields can be assessed against cross sectional images, by identifying the same region in the two volumes based on the presence of the same features, i.e. fibres. For instance, longitudinal displacements in the z-direction are displayed in Figure 4.7 for a longitudinal section in the yz-plane. A part of a fiber is identified and the proposed displacement value is applied in the deformed volume. The identification method shows that ALDVC has high precision in its displacement estimations within the meniscus sample.
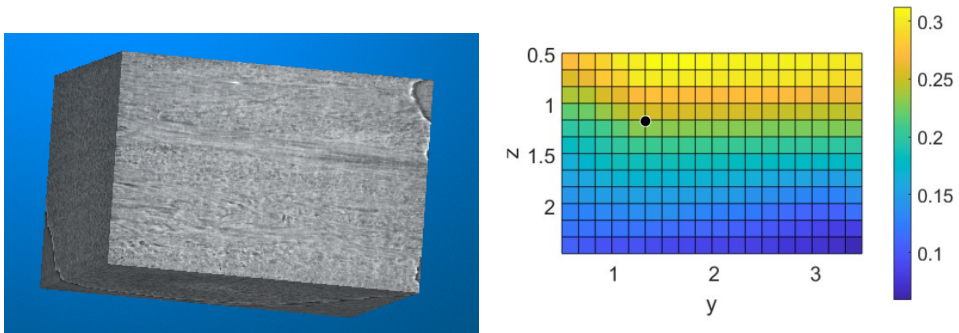
(a) A cross-section 10% into volume 7, parallel to the y- and z-axes.

(b) Z-displacement field in the slice showed in (a). The dimensions and displacement scale are in mm. The node marked with a black dot is located at the edge of a fiber and has a value of 0.23 mm.
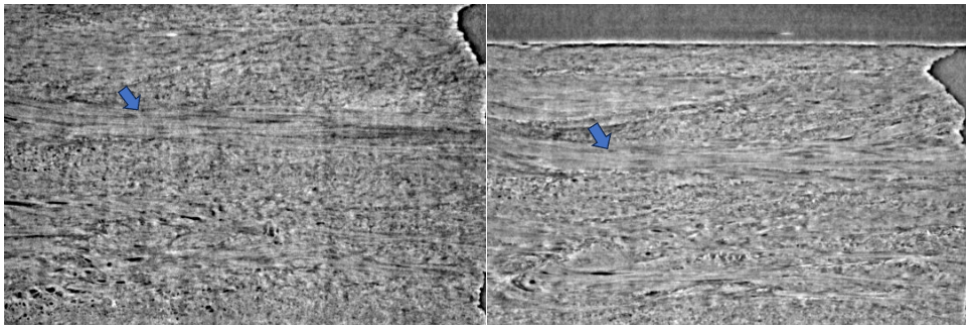
(c) To the left: an orthogonal view of the slice in (a) from volume 7. A blue arrow points at the fiber segment coinciding spatially with the black node in (b). To the right: An image slice in volume 8 corresponding to the estimated x-displacement out of the plane for the fiber segment. The blue arrow shows the displacement estimation in the yz-plane, which is 0.23 mm in z-direction and 0.0048 mm (rougly one pixel) in y-direction. Because of a field pattern similar to 4.6b, the lower-left and upper-right corners in the left slice have experienced larger x-displacements which causes a partial mismatch between the images.

Figure 4.7: Evaluation of displacement results in the first correlation for mensicus 2.

While volume 8 was acquired immediately following the compression, number 15 was acquired after 15 minutes of relaxation. Figure 4.8 shows the computed displacements in

the three orthogonal directions comparing volume 7 and 15. The maximum z-displacement remains nearly the same, with a magnitude of 0.309 mm, and the mean absolute value is also largely unchanged, being 0.213 mm. The mean absolute x- and y-displacements have reduced 29% and 38%, to 0.0299 and 0.0597 mm, respectively. Normal strains for volume pairs 7&8 and 7&15 are visible in Figure 4.9 and Figure 4.10. Since a number of outliers are identified, the 95th percentiles of absolute values is studied instead of actual maximum absolute values, but are still referred to as max-values for simplicity. The max normal z-strain is nearly unchanged between step 8 and 15, mimicking the maximum displacement development. The mean absolute z-strain has a marginal increase, from 0.093 to 0.103. In x- and y-directions there has been a major decrease in this value of 75% and 72%, down from 0.0221 and 0.064.
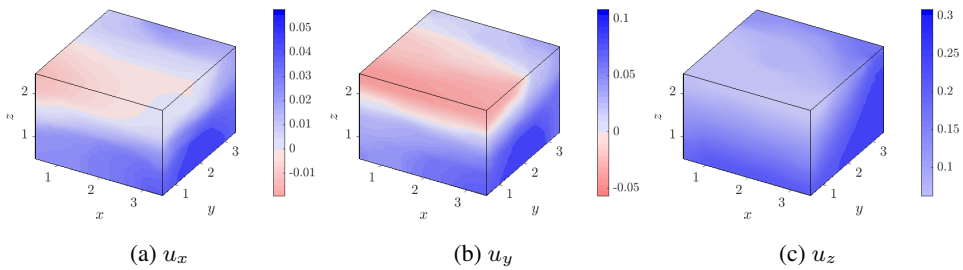

(a) u_x (b) u_y (c) u_z

Figure 4.8: Displacements for ALDVC, time step 7 and 15. Measurements are in mm.

(a) ϵ_{xx} (b) ϵ_{yy} (c) ϵ_{zz}
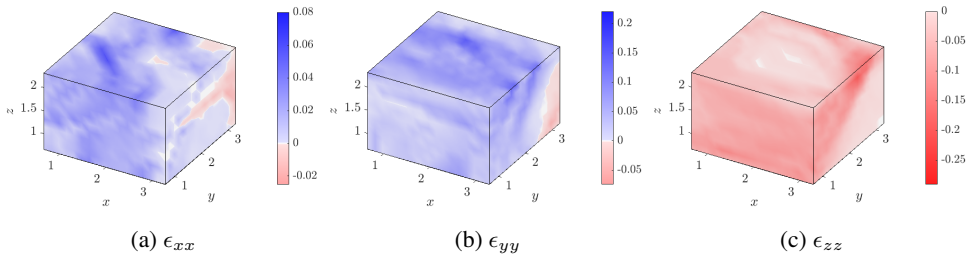
Figure 4.9: Normal strains for meniscus 1 in ALDVC, time step 7 and 8. The VOI dimensions are in mm.

(a) ϵ_{xx} (b) ϵ_{yy} (c) ϵ_{zz}
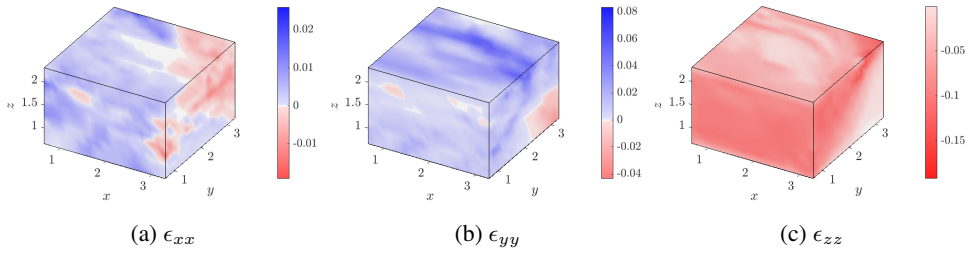
Figure 4.10: Normal strains for ALDVC, time step 7 and 15. The VOI dimensions are in mm.

Next we correlated step 8 (just after compression) to volumes acquired during relaxation: step 12 and 15, which were obtained 100 and 900 seconds after the second strain. The determined displacements between 8 and 12 are displayed in Figure 4.11, and those between 8 and 15 are shown in Figure 4.12. The maximum displacement magnitude between steps 8 and 12, along the z-axis is 0.0341 mm, which is 11% of what was measured between step 7 and 8. The direction of the largest z-deformations is here the opposite, which reflects its relaxation mechanism. The same pattern can be seen for x- and y-displacements, but the maximum in these directions are larger in relation, 32% and 37% respectively. Between step 8 and 15, the maximum value is 72%, 89% and 93% larger than between 8 and 12 in the x-, y-, and z-orientations. This could be expected considering that the relaxation stage has been ongoing for a longer period. The related strains can be viewed in Figure 4.13 and 4.14. Average absolute values in respective orientation are amplified 34%, 74%, and 59% between the two time steps.
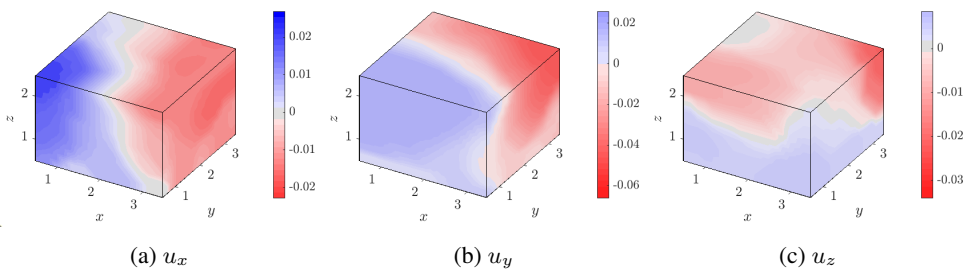

(a) u_x (b) u_y (c) u_z

Figure 4.11: Displacements for ALDVC, time step 8 and 12. All measurements are in mm.

(a) u_x (b) u_y (c) u_z
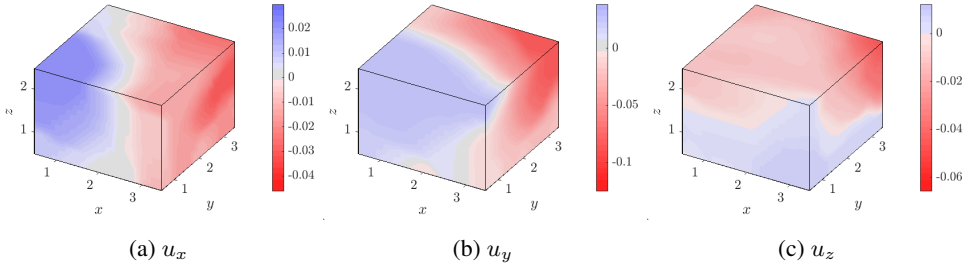
Figure 4.12: Displacements for ALDVC, time step 8 and 15. All measurements are in mm.

(a) ϵ_{xx} (b) ϵ_{yy} (c) ϵ_{zz}
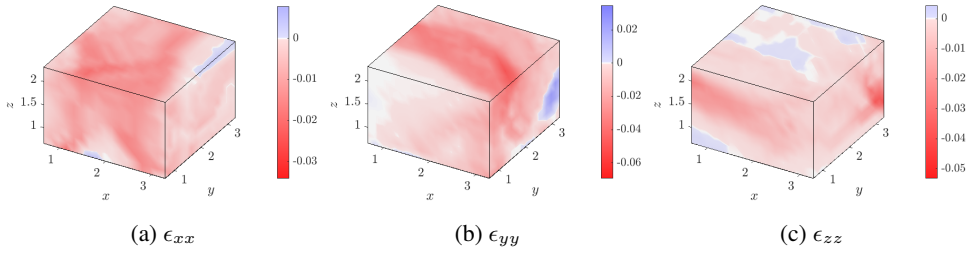
Figure 4.13: Strains for ALDVC, time step 8 and 12. The VOI dimensions are in mm.

(a) ϵ_{xx} (b) ϵ_{yy} (c) ϵ_{zz}
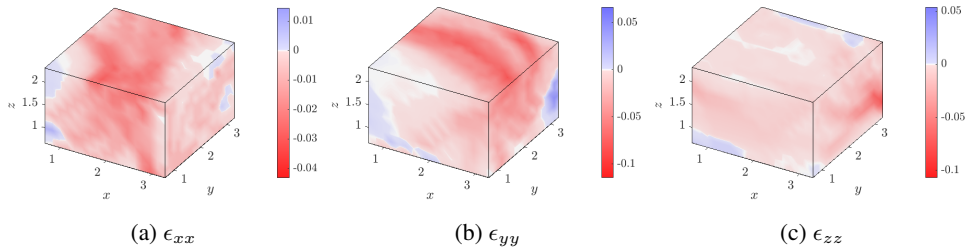
Figure 4.14: Strains for ALDVC, time step 8 and 15. The VOI dimensions are in mm.

There are some convergence issues of varying degree for displacement and strain residuals through the correlation processes. This is illustrated in Figure 4.15, where the residuals of the two local, primal variables and the global, dual displacement field are plotted against each outer iteration step. When performing correlation attempts with a higher maximum iteration number than 7, it can be seen that iteration steps above this number do not improve convergence to a notable extent, taking all four volume pairs into consideration. This means that optimal fields have been practically achieved.
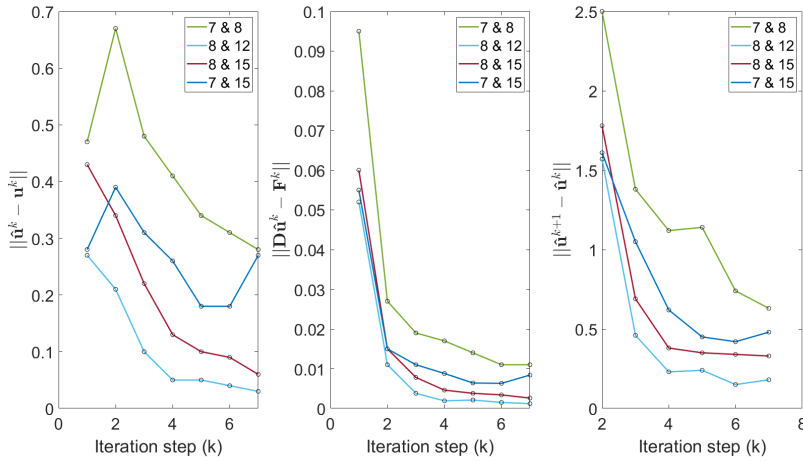
Figure 4.15: Convergences for residuals in all ALDVC procedures for the healthy meniscus (sample 1).

The results for the degenerated meniscus (sample 2) are presented next. Volumes at time step 7 and 8 have been estimated to have a displacement map according to Figure 4.17, and for 7 and 15 the estimation can be found in Figure 4.19. Just as for meniscus 1, z-deformations are fairly unchanged between these two states, with only a 1% decrease for maximum and average values. The more dramatic changes between the correlation results are found in lateral displacements, which have an average maximum reduction of 66%. A comparison of measured displacements and fiber movement for the correlation between volume 7 and 8 is made in Figure 4.16. The tilt of the longitudinal sample axis is smaller compared to the healthy meniscus (sample 1), which becomes evident when studying the displacement fields. The level curves for this sample are more parallel or orthogonal to the transversal plane. A smaller tilt for this sample is likely due to its lower height, which contributes to greater stability during loading.
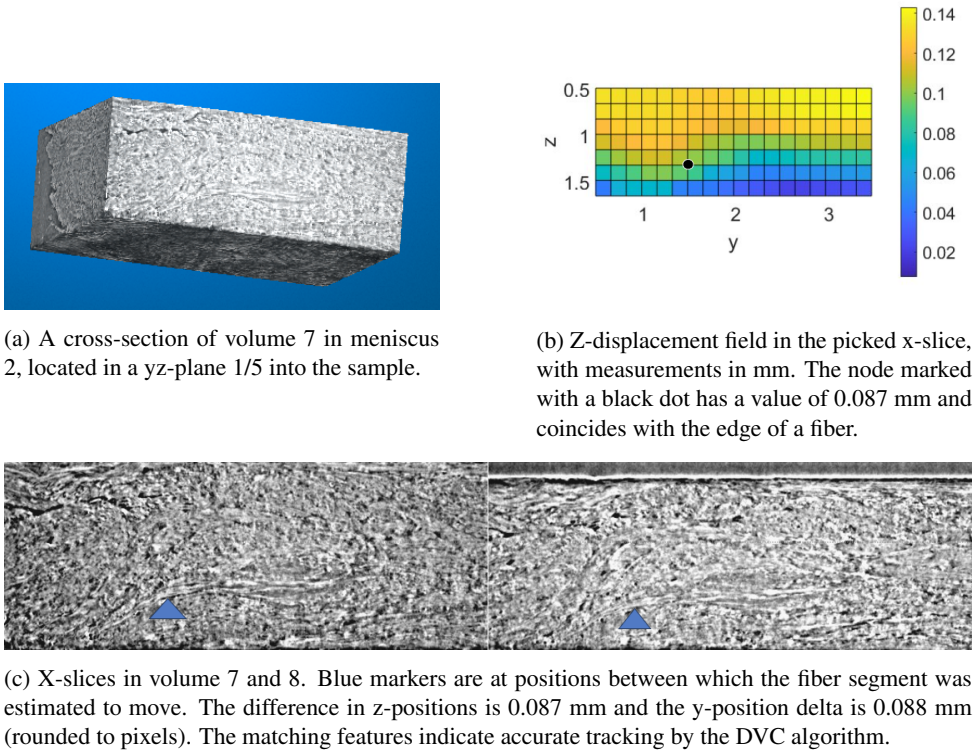
(a) A cross-section of volume 7 in meniscus 2, located in a yz-plane 1/5 into the sample.

(b) Z-displacement field in the picked x-slice, with measurements in mm. The node marked with a black dot has a value of 0.087 mm and coincides with the edge of a fiber.

(c) X-slices in volume 7 and 8. Blue markers are at positions between which the fiber segment was estimated to move. The difference in z-positions is 0.087 mm and the y-position delta is 0.088 mm (rounded to pixels). The matching features indicate accurate tracking by the DVC algorithm.

Figure 4.16: Evaluation of displacement results in the first correlation for mensicus 2.

In Figure 4.20 and 4.21, the associated strains are presented. The evolutions of mean and maximum (95th percentile) values of z-directed strains do not differ largely from the ones for meniscus 1. The mean value has a 4% increase and the maximum a 8% decrease, whereas these values were 11% and 2% for meniscus 1. For each time step meniscus 2 has a slightly higher mean absolute value (18% and 11%) than meniscus 1. In x- and y-directions, the changes are more substantial. Both the mean and max value drop 71%, averaged between the two orientations. The corresponding values for meniscus 1 were 66% for the mean and 74% for the maximum. At time instance 8 the average transversal mean and max strain are 0.037 and 0.075, which is 15% and 10% smaller than for meniscus 1. At instance 15 the mean and max values are 0.011 and 0.022, which is 4% and 28% smaller than for the first meniscus sample.

(a) u_x (b) u_y (c) u_z
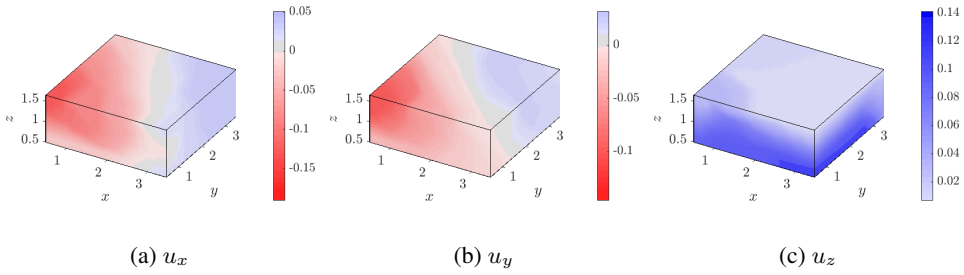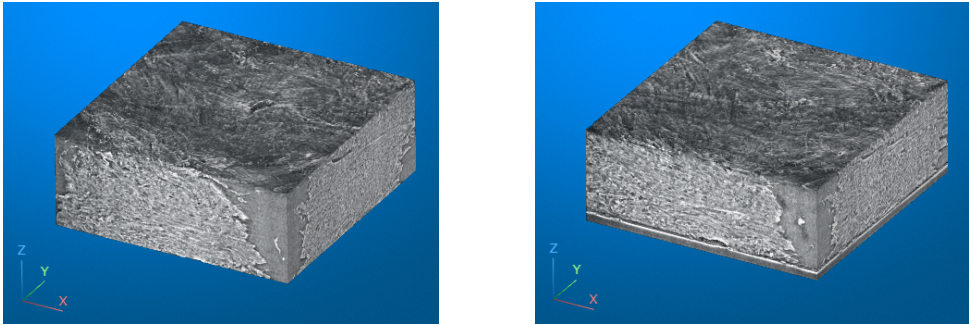
Figure 4.17: Displacements for meniscus 2 (degenerated). The time steps are 7 and 8, and all measurements are in mm. The compression direction is upwards.

(a) State of the sample at time instance 7, im-mediately before stress imposure.

(b) State after stress imposure, time instance 8.
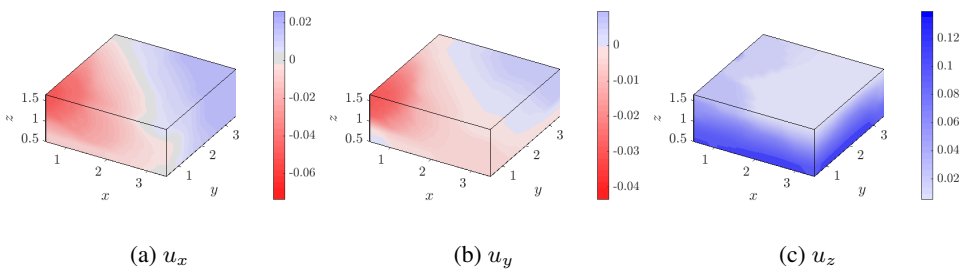
Figure 4.18: Volumes from meniscus 2, step 7 and 8.

(a) u_x (b) u_y (c) u_z

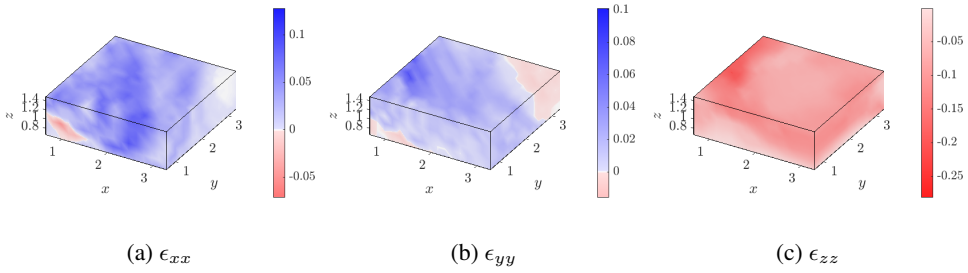Figure 4.19: Meniscus 2 displacements for time steps 7 and 15. All measurements are in mm.

(a) ϵ_{xx} (b) ϵ_{yy} (c) ϵ_{zz}

Figure 4.20: Normal strains for meniscus 2, time step 7 and 8. The VOI dimensions are in mm.

(a) ϵ_{xx} (b) ϵ_{yy} (c) ϵ_{zz}
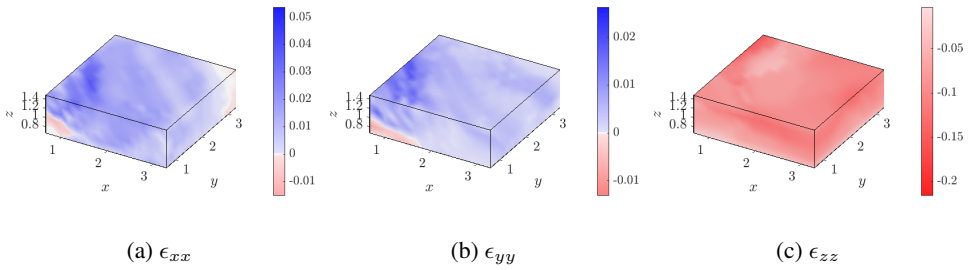
Figure 4.21: Normal strains for meniscus 2, time step 7 and 15. The VOI dimensions are in mm.

In volumes correlated with the state at time step 8, the menisci undergo relaxation and absolute strain metrics therefore increase in all directions between the two correlations with this reference volume. For meniscus 2 the mean and maximum value growth is 82% and 58% longitudinally, as compared to 59% and 51% in meniscus 1. Transversally the mean and max growth is 42% and 48%, and this is a fraction smaller than for meniscus 1, which has a 54% and a 59% increase in these values. The most notable differences between menisci are detected when comparing the individual time steps, and particularly the max values in z-orientation. The two states at step 12 and 15 have a 91% and 84% larger max value for meniscus 1 than for meniscus 2, and respectively 136% and 107% larger mean values. This discrepancy is not as strong laterally, but still influential. The analogous values are 14% and 24% larger maximum, and 20% & 34% larger means.
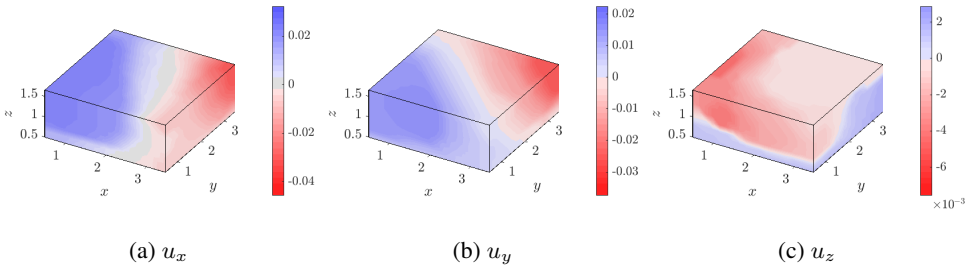
(a) u_x (b) u_y (c) u_z

Figure 4.22: Degenerated meniscus (sample 2) displacements for time steps 8 and 12. All measurements are in mm.

(a) u_x (b) u_y (c) u_z
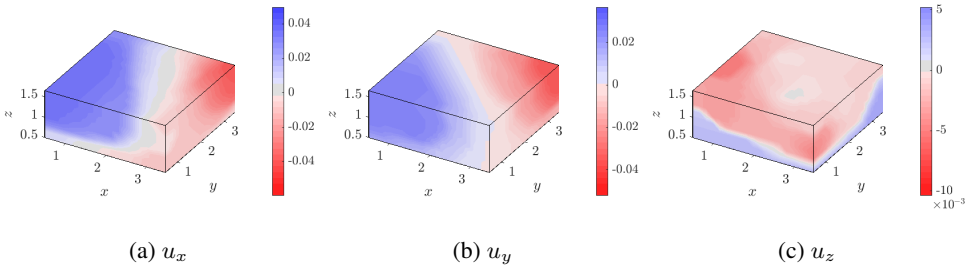
Figure 4.23: Displacements for meniscus 2, time steps 8 and 15. All measurements are in mm.

(a) ϵ_{xx} (b) ϵ_{yy} (c) ϵ_{zz}
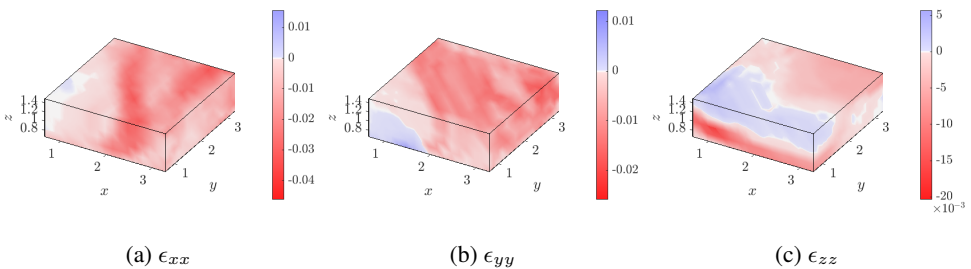
Figure 4.24: Normal strains for meniscus 2, time step 8 and 12. Dimensions of the volume are in mm.

Convergences for meniscus 2 are illustrated in Figure 4.26. In relation to meniscus 1, the convergences in this case are generally stronger. It could be attributed to the fact that sample 1 has a larger height and consequently experience larger deformations.

(a) ϵ_{xx} (b) ϵ_{yy} (c) ϵ_{zz}

Figure 4.25: Normal strains for meniscus 2, time step 8 and 15. The volume dimensions are in mm.
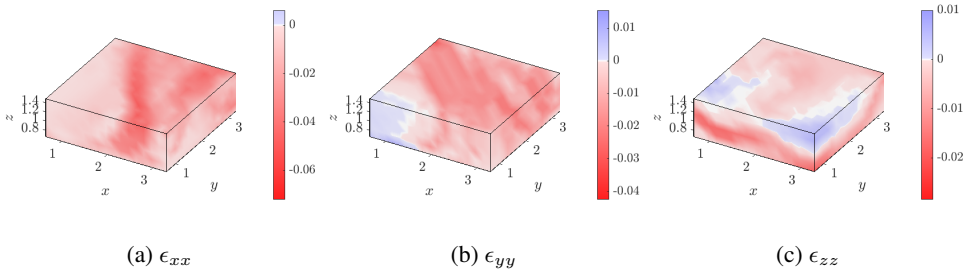

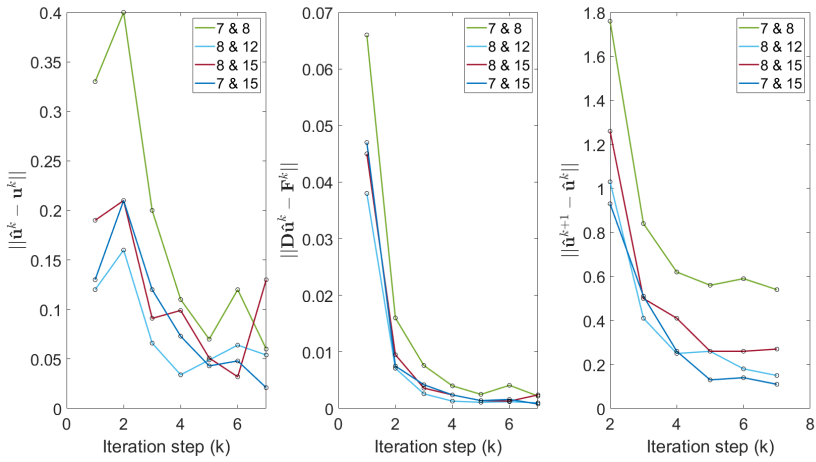Figure 4.26: Convergences for residuals in all ALDVC procedures for the degenerated meniscus (2).

Chapter 5

Discussion

The project aimed to derive deformation maps from μCT tomographs of menisci by using digital volume correlation. Two algorithms, Tomowarp2 and ALDVC, were initially assessed for a set of static sample volumes and the latter was subsequently selected for analysis of uniaxial compression in a strain-controlled testing. Displacements and strains were obtained for one meniscus with no apparent marks of degeneration and one meniscus showing signs of degeneration, during four stages of stress relaxation tests, in the pursuit of characterization and comparison of their mechanical response to the applied pressure. To determine accurate deformation data, a thorough algorithm adaption and parameter optimization was executed.

The processing of zero strain DVC demonstrated clear advantages when using ALDVC. A main concern in the field revolves around identifying well-suited parameters for a given application, making a not excessively high computational cost valuable as it facilitates more efficient adjustments. Another crucial factor influencing the final algorithm choice is the relatively low error rates for ALDVC node strains. Since these errors occured mostly at edges, the initially small VOI did not adequately represent the capabilities of the method. This limitation became apparent when working with larger volumes, which resulted in a substantially lower failure rate. The contrast with Tomowarp was especially evident in this context (see Tables 4.4 and 4.5). Given that the accuracy of ALDVC was universally higher, there was no doubt that this algorithm was the preferable choice to proceed with.

A two-step stress relaxation with 15% and 30% strain each was implemented in the mechanical test. Scan 7 was acquired at the moment before the second load and scan 8 immediately after, while number 12 and 15 were acquired 100s and 900s after the load. Control measures of internal displacements between these volumes in ImageJ reveal accuracy levels of around binned pixel-level (5.50 μm) in computed displacement results. A look at the results for scan 7, 8 and 15 (Figures 4.9, 4.10, 4.20, 4.21) shows how the lateral x- and y-strain magnitudes have decreased largely on average (70 $\sim$ 75%) after 15 minutes of relaxation. It could be ascribed to the dissipation of energy, a characteristic feature of the secondary, time-dependent mechanical response of a viscoelastic material undergoing a physical disturbance [56]. The energy decline is further confirmed by the results for DVC with volume 8 (Figure 4.11 and 4.22), where displacements have essentially turned in the opposite direction, with an increase in the average absolute mean value between scan 12 and 15. The strain decay

in transversal directions aligns with a Maxwell or a Standard Linear Solid (SLS) model but the number of data points over time are too few to fit any parameters for such a model [57]. Changes in the longitudinal displacements are notably less pronounced, due to the confinement of the piston and the bottom plate. The attenuation of energy is thus overwhelmingly manifested laterally by the elastic recovery.

The observed discrepancies in x- and y-directed strains could reasonably be explained by the structural heterogeneity of the samples. Another origin may be traced to anisotropic properties of the meniscus connected to e.g. viscoelasticity. The anisotropic nature is proposed to be an effect of disorderly fibers [40]. Quantifiers for the two transversal directions differ profoundly, hence have they been studied for the directions combined to easier compare between the menisci. The median poisson's ratio for all nodes in this regard in the case of scan 7 & 8 was 0.37 for meniscus 1 and 0.32 for meniscus 2. This result is in accordance with a previous study where a mean ratio of 0.32 ($\pm$ 0.06) for 5 human menisci was obtained [58]. The difference discerned in this study could indicate that the hoop strain generative process is to a degree less effective in meniscus 2. In a study from 2021 it was demonstrated that the stiffness of menisci likely increase with degeneration, which would reasonably correspond with this result [59].

The most noteworthy differences of strains between the two menisci were detected when correlating with the volume immediately after load (8) as the reference (see Figure 4.13, 4.14, 4.24 and 4.25). For meniscus 1 the mean absolute strains were markedly higher, particularly along the longitudinal z-axis. Higher strains in this context are equivalent to a more robust viscoelastic response, and worsening of the viscoelasticity is distinctive for degenerated menisci as a consequence of disruptions in the integrity of collagen [60]. Further is meniscal degeneration linked to increased water content, which in turn correlates with a declining energy dissipation capability [61]. The dissipation of energy is believed to be caused by both friction generated from fluid flow and by time-dependent restructuring of matrix fibers [62]. This means that the identified suboptimal viscoelastic relaxation for meniscus 2 could be contingent on its visible deterioration. Additionally, it has been shown in another thesis that meniscus 1 has a considerably larger outflow of water from fibrils, which would potentially insinuate greater frictional forces and a more intense damping [63].

Dissimilarities in strain results for the correlations with scan 7 as reference (Figure 4.9 and 4.20) are not as strong as the ones with scan 8, but they are still significant. For the longitudinal direction meniscus 2 has larger mean strains, while in the transversal directions they are larger for meniscus 1. The 95% confidence intervals for these, assuming normal distribution, are non-overlapping. This observation coheres with the magnitude order of median Poisson's ratios for scan 7 & 8 (0.37 for meniscus 1 and 0.32 for meniscus 2). The outcomes suggest that meniscus 1 is slightly more efficient in converting compressive stress into tensile stress through outward extrusion.

There is some evidence that a portion of edge nodes are unreliable. A couple of the histograms have a spike of values near zero that deviates from the overall distribution. An exclusion of the outer layer makes the spikes largely diminish and the histograms take on the appearance of a more consistent distribution. Some further relative reduction is achieved when excluding the second outermost layer, but the major effect comes from the first emission. The histograms are provided in the Appendix (6.1 - 6.4). The mean absolute strain

values in the z-direction also converge toward numbers closer to the applied 15% strain with the twofold edge removal. For the larger, healthy meniscus the approach continues by two more exclusions but whether it makes the innermost node values more accurate in general may require a more comprehensive examination. Furthermore, when calculating pointwise values for Poisson's ratio, outliers disappear through the twofold edge-cut procedure and the distribution is narrowing around the median value. Upon visual inspection, it is inferred that potential sources of error primarily stem from the presence of air voids and the edge of the piston, but various types of boundary effects may also contribute.

The Mann-Whitney U-test provides additional pointers to a weighty distinction in relaxation behavior between menisci. Moreover, it reveals some contrast in the initial deformation. While there are apparent visual similarities in strain histograms between the two menisci across all four correlation results (Figure 6.5), an exclusion of the less certain outermost nodes followed by the U-test for all (normal and shear) strains combined gives a significant difference for the correlations with volume 8 as reference. The same practice for the first volume 7 correlation yields a statistically non-significant difference, but when the test is carried out for longitudinal and transversal normal strains separately it shows a significant disparity. As anticipated, the same holds for normal strains in volume 8 correlations.

It is vital to control computed strains relative to the approximated strain resolution from the static DVC. A disproportionately high noise in relation to the actual deformations would make the results substantially more uncertain. The dynamic volume correlation was made with scan times of 5s and the parameters used where $s_{cw} = 30$ and $d_{ns} = 30$ (pixels). The rigid transformation with these parameters for a larger VOI had a standard deviation of absolute strain errors of 0.0047. The mean absolute strains from the dynamic DVC span between 0.0080 and 0.0169 for volume 8 correlations and between 0.0221 and 0.0445 for volume 7 correlations, including both meniscus samples. In the latter case the signal-to-noise ratio is significantly high, while in the second case it is not as strong. When studying each strain type separately, a few of the smallest deformation instances have a signal-to-noise ratio (μ/σ) around 1. This could possibly introduce some uncertainty to those results, but noise reduction methods as average pixel downsampling and gaussian smoothing of displacement fields have been used. In addition, the global kinematic compatibility of the ALDVC algorithm is expected to provide robustness to noise and artefacts. It is also conceivable that the error assigned to rigid translation is slightly overrated due to a not entirely flawless registration performance.

Another aspect in the outcome evaluation is convergences, both for displacement components during the inner loop (ICGN) process and between steps in the outer loop (ADMM). For the last, seventh ADMM iteration step, the highest rate of non-converged nodes was achieved for meniscus 1, having 5.1% and 5.2% for scan 8 against scan 7 respectively scan 15. For the other six correlations, the mean percentage was 1.7. These are somewhat low numbers that the method should handle quite effortlessly with the global compatibility step. In the ADMM loop, none of the correlation optimization runs actually converged in the strict sense of having the displacement residual norm below the threshold of 10^{-2}. Nevertheless, there is a clear pattern of convergence in all 8 cases, for both primal and dual variables (see Figure 4.15 and 4.26). The highest residuals are retrieved from scan 7 and 8 correlation for meniscus 1, which is rational since the largest deformations have occurred between these. The residuals are in general small relative to displacements. A couple of the

displacement residual curves have a mild upswing in the last step. The parameter optimization was made for all eight volume pairs together and this shows that there is a potential to improve individual results by tailor-made tuning.

5.1 Limitations and future directions

A primary shortcoming of this study is the fact that only two menisci are studied, one that shows signs of degeneration and one that does not. Although significant differences in strains were shown, the findings may have limited generalization to a broader population and should therefore be interpreted with caution. The objective of this project was mainly to develop the pipeline for strain calculation, but future studies with a broader sample collection are motivated to enhance the robustness in the comparative analysis that was performed. In particular, degeneration in the meniscus can manifest in various ways, and the complexity of these different conditions could warrant further investigation.

The number of deformed volumes correlated with the reference volumes is possibly low, and does not fully capture potentially nuanced changes occurring within the material. Since volumes of meniscus states from intermediate time points relative to those used in this project are available, it would be beneficial to extend the exploration to include these volumes. It would provide a more comprehensive understanding of stress relaxation dynamics and would facilitate the identification of trends and presumed non-linearities. Particullarly it would augment the possibilities of fitting viscoelastic models, such as the Maxwell model, to the data.

Furthermore, a direct comparison with the yield strain is not feasible as the results exclusively involve strains from the second compression in the experiment. A tomogram of the meniscus state prior to the initial compression is presently unavailable. However, the results strongly suggest that a predominant share of the tissue is still within the elastic region as the 95th percentiles of absolute strains have reduced 66% and 71% in the unbounded orientations after 15 minutes of relaxation. A more detailed examination of the yield strain relationship could be considered in prospective analyses.

The compression piston utilized had a flat surface, as contrasted to the more rounded femoral condyles that interact with the meniscus in vivo. This design results in the loss of a horizontal force component, and to better replicate the biomechanical reality, adjustments to the piston should be considered. Furthermore, the implementation of different load protocols would be valuable. The current protocol physically corresponds to a single vertical jump or lifting a heavy weight, while simulation of repetitive movements like walking, running, or cycling would require a periodic model and matching load appliance. Another difference from in vivo conditions is the absence of the thin outermost layer of randomly organized fibers laterally in the cylinder-shaped samples compared to the intact meniscus. This suggests that strains in those directions may be somewhat overestimated in relation to what would occur in vivo.

An alternative parameter optimization approach to the one implemented in this project would be to do Bayesian optimization. The Bayesian optimization procedure would treat the DVC algorithm as a black box, and systematically adjust parameters based on the al-

gorithm's performance without explicit knowledge of its internal structure. Specifically it could facilitate the process of obtaining an optimized set of parameters for all volume pairs involved. One possible drawback is if the problem turns out to be non-stationary. In such cases, more sophisticated models beyond the standard Gaussian process framework might be necessary [64].

5.2 Ethical aspects

The human meniscus samples in the thesis came from the MENIX biobank (PI. Collaborator Prof M. Englund) where menisci without any known degeneration were taken from deceased donors, and degenerated menisci were donated from patients who had received knee replacement surgery. The bovine meniscus sample was harvested from livestock already slaughtered for other purposes. The human samples were all anonymized to ensure privacy. Furthermore, there was no risk of radiation damage to living individuals since the imaging was conducted ex vivo. The acquired tomograms are accessible for future applications, which reduces the need for additional human tissue. This is particularly crucial as the extraction of plugs causes irreversible damage to the meniscus. The findings of this project could provide valuable insights into biomechanics and its correlation with diseases of the human meniscus.

5.3 Conclusions

ALDVC is a more suitable choice for analyzing strains in the SXR-PhC-μCT meniscus data compared to Tomowarp2. Its accuracy and precision is higher, and it has a substantially lower node error rate across all VOI sizes. Furthermore, ALDVC's low computational cost allows for efficient parameter adjustments, which enhances flexibility in the analysis routine.

The intrinsic noise of the system including the ALDVC algorithm and the meniscus volumes is comfortably below the mean strain magnitudes in deformation scenarios relative to the volume before load (7). In correlations with volume 8 (immediately after load) care should be exercised since a few strain component means are at the same level as the noise. However, for the correlation instances in this project, noise reduction efforts such as pixel binning, enforced kinematic compatibility and displacement smoothing prove to be successful based on the manual tracking and residual convergences.

The menisci differ significantly in both initial and secondary responses. For the healthy meniscus, the Poisson effect appears to be stronger and a more effective lateral expansion materializes immediately after load. In the relaxation phase, the healthy meniscus exhibits a notably higher level of viscoelastic damping, resulting in faster tissue recovery compared to the degenerated meniscus. This distinction is particularly evident in the mean magnitude strains in the axial direction, where the two menisci show the most significant difference. The less robust responses of the degenerated meniscus could be attributed to lower efficiency in strain transferability and energy attenuation. Both these characteristics are commonly observed in degenerated menisci.

Correlation analysis should be prospectively extended to volumes with intermediate time stamps and to an expanded number of meniscus samples. This will enable a more thorough investigation of the strain development during stress relaxation and its association with different health conditions of menisci. There might also be an opportunity to enhance strain accuracy, such as through the implementation of a Bayesian optimization framework. This system could optimize parameters by simultaneously taking all included volume pairs into account.

Bibliography

[1] J. L. Cook *et al.*, "Meniscal biology in health and disease," *Connective Tissue Research*, vol. 58, no. 3-4, pp. 225–237, 2017.

[2] N. Ozeki, H. Koga, and I. Sekiya, "Degenerative meniscus in knee osteoarthritis: From pathology to treatment," *Life*, vol. 12, no. 4, p. 603, 2022.

[3] M. Englund, A. Guermazi, and L. S. Lohmander, "The meniscus in knee osteoarthritis," *Rheumatic Disease Clinics of North America*, vol. 35, no. 3, pp. 579–590, August 2009.

[4] S. Glyn-Jones *et al.*, "Osteoarthritis," *The Lancet*, vol. 386, no. 9991, pp. 376–387, 2015.

[5] H. Long, Q. Liu, H. Yin, K. Wang, N. Diao, Y. Zhang, J. Lin, and A. Guo, "Prevalence trends of site-specific osteoarthritis from 1990 to 2019: Findings from the global burden of disease study 2019," *Arthritis & Rheumatology*, vol. 74, no. 7, pp. 1172–1183, July 2022.

[6] E. Einarsson, M. Pierantoni, V. Novak, J. Svensson, H. Isaksson, and M. Englund, "Phase-contrast enhanced synchrotron micro-tomography of human meniscus tissue," *Osteoarthritis and Cartilage*, vol. 30, no. 9, pp. 1222–1233, 2022. [Online]. Available: https://www.sciencedirect.com/science/article/pii/S1063458422007671

[7] Z. Izadifar, A. Honaramooz, S. Wiebe, G. Belev, X. Chen, and D. Chapman, "Low-dose phase-based x-ray imaging techniques for in situ soft tissue engineering assessments," *Biomaterials*, vol. 82, pp. 151–167, Mar 2016.

[8] L. Grassi and H. Isaksson, "Extracting accurate strain measurements in bone mechanics: A critical review of current methods," *Journal of the Mechanical Behavior of Biomedical Materials*, vol. 50, pp. 43–54, 2015.

[9] C. Disney, A. Eckersley, J. McConnell, H. Geng, A. Bodey, J. Hoyland, P. Lee, M. Sherratt, and B. Bay, "Synchrotron tomography of intervertebral disc deformation quantified by digital volume correlation reveals microstructural influence on strain patterns," *Acta Biomaterialia*, vol. 92, pp. 290–304, 2019.

[10] B. C. Roberts, E. Perilli, and K. J. Reynolds, "Application of the digital volume correlation technique for the measurement of displacement and strain fields in bone: A literature review," *Journal of Biomechanics*, vol. 47, pp. 923–934, 2014.

[11] B. D. Chaurasia, *Human Anatomy: Regional and Applied Dissection and Clinical: Lower Limb Abdomen and Pelvis (Vol. 2)*, 6th ed.   CBS Publishers and Distributors Pvt Ltd, 2015.

[12] "Normal knee anatomy," Retrieved from OrthoInfo: https://orthoinfo.aaos.org/en/diseases–conditions/discoid-meniscus, image source: American Academy of Orthopaedic Surgeons.

[13] P. R. Kurzweil, "Three types of collagen fibers," Retrieved from Musculoskeletal Key: https://musculoskeletalkey.com/inside-out-and-outside-in-meniscus-repair/.

[14] A. A. Allen, G. L. Caldwell Jr, and F. H. Fu, "Anatomy and biomechanics of the meniscus," *Operative Techniques in Orthopaedics*, vol. 5, no. 1, pp. 2–9, January 1995.

[15] J. S. Bell *et al.*, "Tropocollagen springs allow collagen fibrils to stretch elastically," *Acta Biomaterialia*, vol. 142, pp. 185–193, April 2022.

[16] M. Fang *et al.*, "Type i collagen d-spacing in fibril bundles of dermis, tendon and bone: Bridging between nano- and micro-level tissue hierarchy," *ACS Nano*, vol. 6, no. 11, pp. 9503–9514, Nov 2012.

[17] E. S. Mameri, S. P. Dasari, L. M. Fortier, F. Gómez Verdejo, S. Gursoy, A. B. Yanke, and J. Chahla, "Review of meniscus anatomy and biomechanics," *Current Reviews in Musculoskeletal Medicine*, vol. 15, no. 5, pp. 323–335, Oct 2022.

[18] A. J. Fox, F. Wanivenhaus, A. J. Burge, R. F. Warren, and S. A. Rodeo, "The human meniscus: A review of anatomy, function, injury, and advances in treatment," *Clinical Anatomy*, vol. 28, pp. 269–287, 2015.

[19] S. Varma, J. P. R. O. Orgel, and J. D. Schieber, "Nanomechanics of type i collagen," *Biophysical Journal*, vol. 111, no. 1, pp. 50–56, July 2016.

[20] A. L. McNulty and F. Guilak, "Mechanobiology of the meniscus," *J Biomech*, vol. 48, no. 8, pp. 1469–1478, Jun 1 2015.

[21] J. M. Peloquin, M. H. Santare, and D. M. Elliott, "Advances in quantification of meniscus tensile mechanics including nonlinearity, yield, and failure," *J Biomech Eng*, vol. 138, no. 2, pp. 0 210 021–02 100 213, Feb 2016.

[22] E. Danso, J. Honkanen, S. Saarakkala, and R. Korhonen, "Comparison of nonlinear mechanical properties of bovine articular cartilage and meniscus," *Journal of Biomechanics*, vol. 47, no. 1, pp. 200–206, 2014. [Online]. Available: https://doi.org/10.1016/j.jbiomech.2013.09.015

[23] D. J. Hunter and S. Bierma-Zeinstra, "Osteoarthritis," *The Lancet*, vol. 393, pp. 1745–1759, 2019.

[24] R. Sen and J. A. Hurley, "Osteoarthritis," *StatPearls*, 2023, updated 2023 Feb 20. [Online]. Available: https://www.ncbi.nlm.nih.gov/books/NBK482326/

[25] Osteoarthritis (degenerative arthritis). Michigan Medicine, University of Michigan Health. Accessed 2023-11-25. [Online]. Available: https://www.uofmhealth.org/conditions-treatments/cmc/arthritis/osteoarthritis

[26] S. N. Ahmed, *Physics and Engineering of Radiation Detection (Second Edition)*. Elsevier, 2015.

[27] M. Chappell, *Principles of Medical Imaging for Engineers: From Signals to Images*. Springer, 2019.

[28] G. A. Hay, "X-ray imaging," *Journal of Physics E: Scientific Instruments*, vol. 11, no. 5, p. 377, 1978.

[29] Micro-computed tomography. Accessed on 2023-11-25. [Online]. Available: https://sites.research.unimelb.edu.au/tracees/capabilities/geo-node/micro-ct

[30] A. du Plessis, C. Broeckhoven, A. Guelpa, and S. G. le Roux, "Laboratory x-ray micro-computed tomography: a user guideline for biological samples," *Gigascience*, vol. 6, no. 6, pp. 1–11, 2017.

[31] S. Cheriyedath. (N/A) Micro-ct principles, strengths, and weaknesses. Reviewed by Dr. Liji Thomas, MD. Last Updated: Jul 24, 2023. [Online]. Available: https://www.news-medical.net/life-sciences/Micro-CT-Principles-Strengths-and-Weaknesses.aspx

[32] M. Tamal, M. Althobaiti, A.-H. Alomari, S. T. Dipty, K. T. Suha, and M. Al-Hashim, "Synchrotron x-ray radiation (sxr) in medical imaging: Current status and future prospects," *Applied Sciences*, vol. 12, no. 8, p. 3790, 2022.

[33] F. Mücklich and H. Yao, "Metallic and nonmetallic x-ray monochromators for synchrotron sources," *Current Opinion in Solid State and Materials Science*, vol. 2, pp. 311–317, 1997.

[34] A. C. Thompson and J. Llacer, "Computed tomography using synchrotron radiation," *Nuclear Instruments and Methods in Physics Research*, vol. 222, pp. 319–323, 1984.

[35] B. D. Metscher, "Microct for comparative morphology: simple staining methods allow high-contrast 3d imaging of diverse non-mineralized animal tissues," *BMC Physiology*, vol. 9, no. 1, p. 11, 2009.

[36] S. Mayo, A. Stevenson, and S. Wilkins, "In-line phase-contrast x-ray imaging and tomography for materials science," *Materials*, vol. 5, no. 5, pp. 937–965, 2012. [Online]. Available: https://doi.org/10.3390/ma5050937

[37] J. Keyriläinen, A. Bravin, M. Fernandez, M. Tenhunen, P. Virkkunen, and P. Suortti, "Phase-contrast x-ray imaging of breast," *Acta Radiologica*, vol. 51, no. 8, pp. 866–884, 2010.

[38] N. Kishev, J. S. Kang, and K. Moon, "Techniques for characterizing mechanical properties of soft tissues," *Journal of the Mechanical Behavior of Biomedical Materials*, vol. 138, 2023. [Online]. Available: https://doi.org/10.1016/j.jmbbm.2022.105575

[39] C. Ljung, N. S. Ottosen, and M. Ristinmaa, *Introduktion till hållfasthetslära: enaxliga tillstånd*, 1st ed. Studentlitteratur AB, 2007.

[40] A. Gabrion, P. Aimedieu, Z. Laya *et al.*, "Relationship between ultrastructure and biomechanical properties of the knee meniscus," *Surgical and Radiologic Anatomy*, vol. 27, no. 6, pp. 507–510, 2005.

[41] V. Alekna, O. Ardatov, J. Selivonec, and O. Chabarova, "In silico modeling the impact of cartilage stiffness on bone tissue stress," *Applied Sciences*, vol. 13, 2023. [Online]. Available: https://doi.org/10.3390/app13074457

[42] D. Rees, *Basic Engineering Plasticity: An Introduction with Engineering and Manufacturing Applications*, 1st ed.   Butterworth-Heinemann, 2006.

[43] J. Yang, L. Hazlett, A. Landauer *et al.*, "Augmented lagrangian digital volume correlation (aldvc)," *Experimental Mechanics*, vol. 60, pp. 1205–1223, 2020. [Online]. Available: https://doi.org/10.1007/s11340-020-00607-3

[44] Digital volume correlation. Accessed on 4th February 2024. [Online]. Available: https://www.franck.engr.wisc.edu/digital-volume-correlation

[45] E. Tudisco *et al.*, "Tomowarp2: Measuring 3d displacement fields through digital volume correlation," in *3rd International Conference on Tomography of Materials and Structures*.   Lund, Sweden: Lund University - Department of Construction Sciences, Lund, Sweden and University Grenoble Alpes, 3SR, F-38000, Grenoble, France, 2017.

[46] E. Tudisco, E. Andò, R. Cailletaud, and S. A. Hall, "Tomowarp2: A local digital volume correlation code," *SoftwareX*, vol. 6, pp. 267–270, 2017. [Online]. Available: https://doi.org/10.1016/j.softx.2017.10.002

[47] A. Goyal and G. W. Melenka, "Investigation of carbon-aramid hybrid braided composites using digital volume correlation," *Composite Structures*, vol. 321, 2023.

[48] J. Eckstein and D. Bertsekas, "On the douglas—rachford splitting method and the proximal point algorithm for maximal monotone operators," *Mathematical Programming*, vol. 55, pp. 293–318, 1992.

[49] J. Nocedal and S. J. Wright, *Numerical Optimization*, 2nd ed.   Berlin, New York: Springer-Verlag, 2006.

[50] "Run Code on Parallel Pools," https://se.mathworks.com/help/parallel-computing/run-code-on-parallel-pools.html, 2023, accessed: February 29, 2024.

[51] J. Yang, L. Hazlett, A. Landauer, and C. Franck, *Augmented Lagrangian Digital Volume Correlation (ALDVC) Code Manual (v1.0)*, Madison, WI, USA, 2020.

[52] E. H. R. Tsai, F. Marone, and M. Guizar-Sicairos, "Gridrec-ms: an algorithm for multi-slice tomography," *Optics Letters*, vol. 44, pp. 2181–2184, 2019.

[53] P. D. et. al., "Phase retrieval using coherent imaging systems with linear transfer functions," *Optics Communications*, vol. 234, pp. 87–105, 2004.

[54] C. A. Schneider, W. S. Rasband, and K. W. Eliceiri, "Nih image to imagej: 25 years of image analysis," *Nature Methods*, vol. 9, no. 7, pp. 671–675, 2012.

[55] M. A. Sutton, J.-J. Orteu, and H. W. Schreier, *Image correlation for Shape, Motion and Deformation Measurements*.   Springer, 2009.

[56] O. Chaudhuri, J. Cooper-White, P. A. Janmey, D. J. Mooney, and V. B. Shenoy, "Effects of extracellular matrix viscoelasticity on cellular behaviour," *Nature*, vol. 584, no. 7822, pp. 535–546, 2020.

[57] D. Roylance, *Engineering Viscoelasticity*. Cambridge, MA 02139: Department of Materials Science and Engineering, Massachusetts Institute of Technology, 2001.

[58] A. Morejon *et al.*, "Compressive properties and hydraulic permeability of human meniscus: Relationships with tissue structure and composition," *Frontiers in Bioengineering and Biotechnology*, vol. 8, 2021.

[59] A. M. Seitz *et al.*, "Osteoarthritis-related degeneration alters the biomechanical properties of human menisci before the articular cartilage," *Frontiers in Bioengineering and Biotechnology*, vol. 9, 2021. [Online]. Available: https://www.frontiersin.org/articles/10.3389/fbioe.2021.659989

[60] D. Warnecke *et al.*, "Degeneration alters the biomechanical properties and structural composition of lateral human menisci," *Osteoarthritis and Cartilage*, vol. 28, pp. 1482–1491, 2020.

[61] A. Morejon, A. Mantero, T. Best, A. Jackson, and F. Travascio, "Mechanisms of energy dissipation and relationship with tissue composition in human meniscus," *Osteoarthritis and Cartilage*, vol. 30, pp. 605–612, 2022.

[62] A. Morejon *et al.*, "Tensile energy dissipation and mechanical properties of the knee meniscus: relationship with fiber orientation, tissue layer, and water content," *Frontiers in Bioengineering and Biotechnology*, vol. 11, 2023.

[63] M. Abrahamsson, "Using a semi-automatic layer detection algorithm to determine collagen fiber alignment in the human meniscus during loading." Master's thesis, Lund University, Lund, Sweden, 2023.

[64] J. Snoek *et al.*, "Input warping for bayesian optimization of non-stationary functions," in *Proceedings of the 31st International Conference on Machine Learning*, vol. 32. PMLR, 2014, pp. 1674–1682.
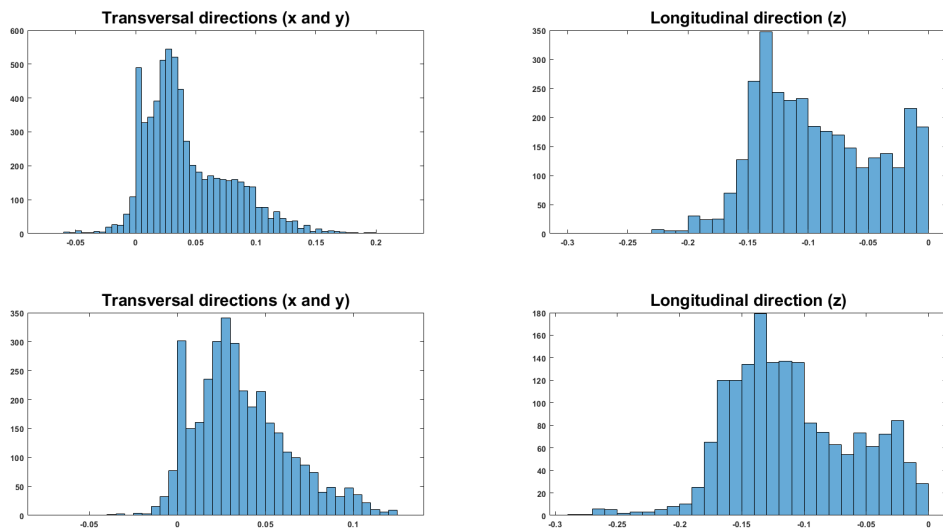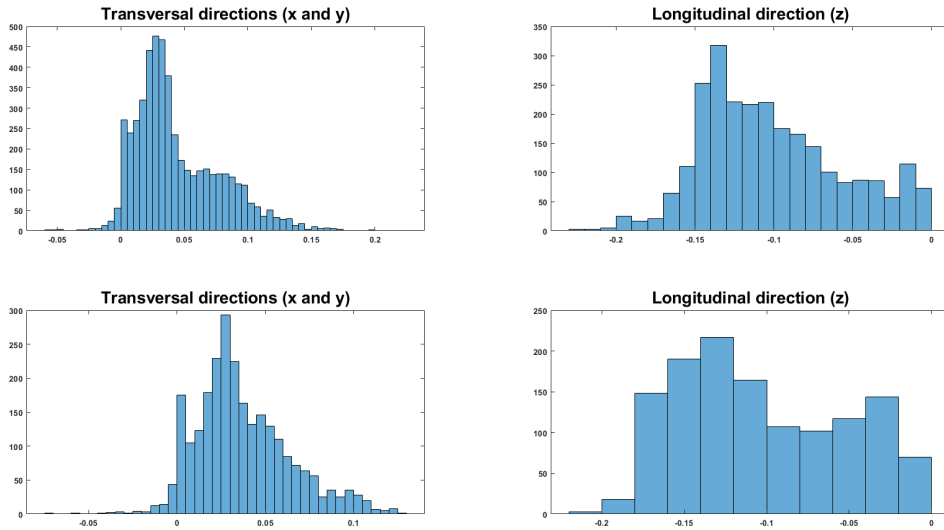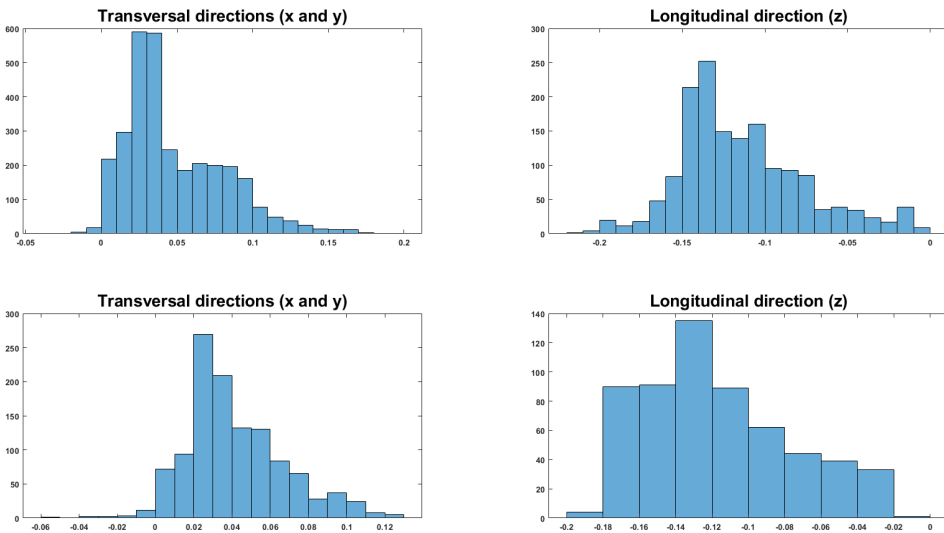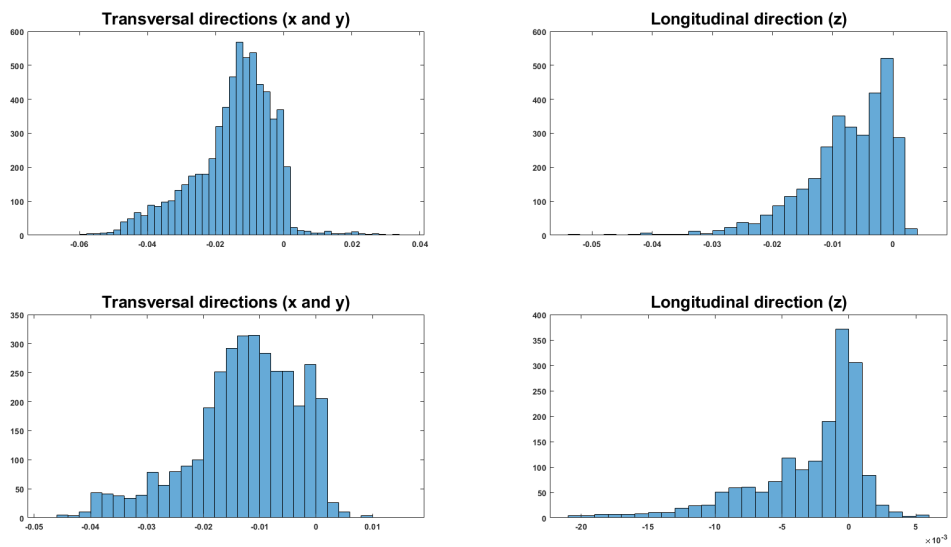
Appendix

6.1 Strain histograms

Figure 6.1: Histograms for the normal strains in the correlation between volume 7 and 8. The upper row is for sample 1 and the lower row is for sample 2.

(a) Histograms after exlusion of the outer layer.

(b) Histograms after exlusion of the two outermost layers.

Figure 6.2: Histograms for the normal strains in the correlation between volume 7 and 8, after excluding node layers. The upper rows are for sample 1 and the lower rows are for sample 2.

Figure 6.3: Histograms for the normal strains in the correlation between volume 8 and 12. The upper row is for sample 1 and the lower row is for sample 2.
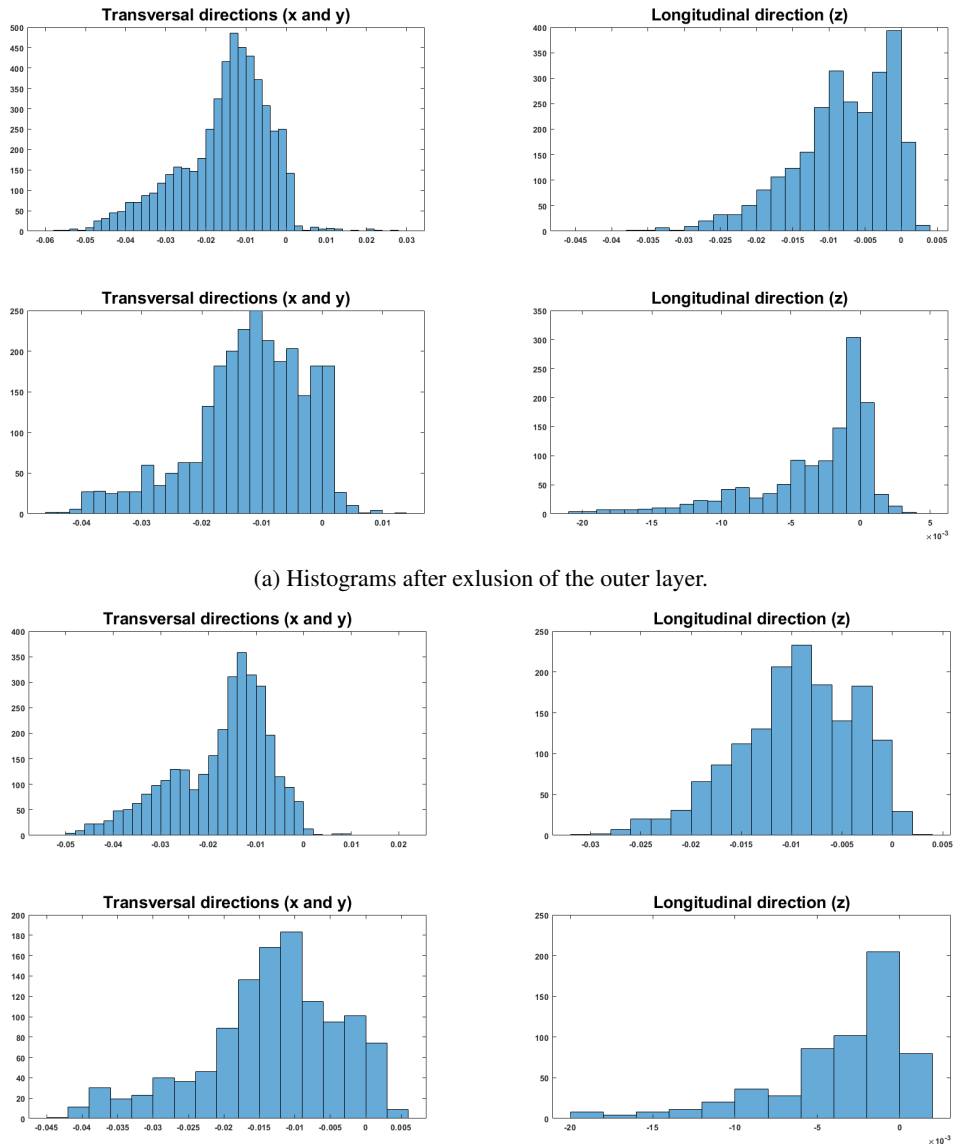
(a) Histograms after exlusion of the outer layer.

(b) Histograms after exlusion of the two outermost layers.

Figure 6.4: Histograms for the normal strains in the correlation between volume 8 and 12, after excluding node layers. The upper rows are for sample 1 and the lower rows are for sample 2.
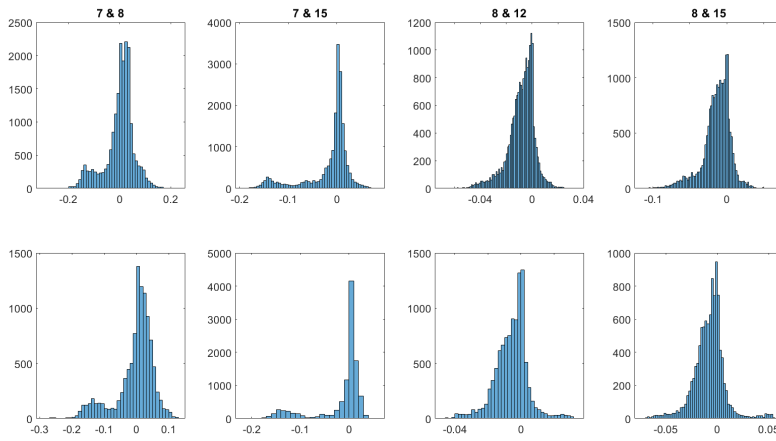
Figure 6.5: Histograms for all strains (normal and shear) in each correlation. The upper row is for sample 1 and the lower row is for sample 2.
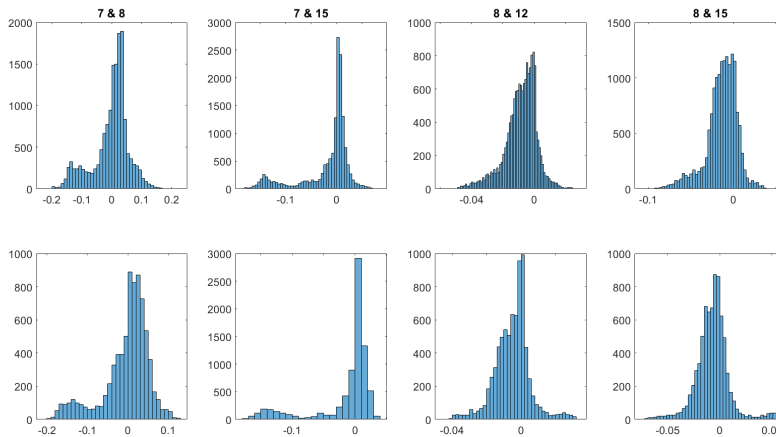

Figure 6.6: Histograms for all strains (normal and shear) in each correlation, after the exclusion of the outer node layer. The upper row is for sample 1 and the lower row is for sample 2.